

0017
22361
P-79

ELASTIC PLASTIC FRACTURE MECHANICS METHODOLOGY FOR SURFACE CRACKS

SEMIANNUAL REPORT
CONTRACT MSFC CONTROL NO. 91-78

N95-11583

Unclas

G3/39 0022361

NASA MARSHALL SPACE FLIGHT CENTER
HUNTSVILLE, AL 35812

Project Monitor:

Mr. Wayne Gregg

Principal Investigator:

Dr. Hugo A. Ernst
Associate Professor

Researcher:

D. M. Lambert

(NASA-CR-196811) ELASTIC PLASTIC
FRACTURE MECHANICS METHODOLOGY FOR
SURFACE CRACKS Semiannual Report, of
Mar. - Aug. 1994 (Georgia Inst. of
Tech.) 94 p

GEORGIA INSTITUTE OF TECHNOLOGY
THE GEORGE W. WOODRUFF SCHOOL OF MECHANICAL ENGINEERING
Atlanta, GA 30332-0405

August 1994

INDEX

1.	Introduction	
1.1	General.....	1.3
1.2	Elastic Plastic Fracture Mechanics.....	1.4
1.3	The Leak Before Burst (LBB) Criterion.....	1.6
1.4	This Project.....	1.8
1.5	This Report.....	1.11
1.6	References for Chapter 1.....	1.13
1.7	Figures for Chapter 1.....	1.14
2.	<i>Efforts to Characterize Three-Dimensional Effects Observable in Two Dimensional Fracture Specimens</i>	
2.1	Introduction.....	2.1
2.2	Introduction to Profiling.....	2.3
2.3	Profiling Matrix and Details.....	2.5
2.4	Profiling Results.....	2.6
2.5	Initiation Stretch.....	2.17
2.6	Conclusions and Recommendations.....	2.23
2.7	References for Chapter 2.....	2.25
2.8	Tables for Chapter 2.....	2.26
2.9	Figures for Chapter 2.....	2.30
3.	Resistance Curve Analysis	
3.1	J and J_M Resistance Curve Analysis.....	3.1
3.2	Power-Law Fit of R-Curve Data and J_{IC} Estimates.....	3.13
3.3	Conclusions and Recommendations.....	3.17
3.4	References for Chapter 3.....	3.20
3.5	Tables for Chapter 3.....	3.21
3.6	Figures for Chapter 3.....	3.23

1. Introduction

1.1 General

The safety and reliability of structures has always been a matter of vital concern to the aerospace industry. In this respect, fracture mechanics (FM) is an especially useful technology, since it can provide a quantitative description of the capability of structural parts to tolerate flaws. Initially, FM concepts covered quasi-linear elastic conditions (LEFM). Later, these methods were further developed to cover more general situations: a need existed to extend LEFM concepts to include cases where yielding was not necessarily contained in very small regions. This is often the case for new and tougher materials subjected to higher loads and used in thinner sections. This led to the development of the Elastic Plastic Fracture Mechanics (EPFM) Methodology.

To apply these methods, two pieces of information are needed: the so-called material/specimen response to deformation, and the material response to crack extension. The former, obtained by finite element analysis or experimental calibration, consists of two expressions connecting the J-integral, load P , load-point displacement v , and crack length a for the specimen geometry of interest; the latter consists of a characterization of the way the

material resists crack extension for the type of load applied: J , or a similar parameter, versus crack extension, for monotonic load, da/dN versus ΔK or ΔJ for cyclic loading, or da/dt versus K , C^* or C_t for creep crack growth. Within certain limitations, these curves are assumed to be specimen geometry independent, i.e., the curve obtained from a small laboratory specimen applies to the structural part under consideration, as well.

A simple computer program can be developed to combine the two pieces of information mentioned and assess the reliability of the structural part of interest.

It is very important to verify that the curve of material response to crack extension is geometry independent: the limitations of the parameters and/or approaches used must be understood, their validity limits must be clearly identified with the goals of improving the characterization of the phenomenon and proposing new parameters and methods to extend the range of applicability of existing models.

1.2 Elastic Plastic Fracture Mechanics

Specifically, for the case of EPFM applied to monotonic load, the mentioned limitations are expressed in terms of the amount of crack extension to ligament ratio, r , the

ratio of ligament to applied J over the yield strength, m , and the ratio of logarithmic increase of J to logarithmic decrease in ligament, ω .

To overcome some of these limitations, particularly the one on r , Ernst [1.1] proposed a modified version of J called J_M . Resistance (R) curves plotted in terms of J_M were not subjected to the same limitations as those using J , and in general, showed a better correlation between specimens of different size and geometry.

More recently, this methodology was further extended: general formulas were developed for J_M and J_D for growing cracks, criteria were proposed to identify the limits of applicability of both parameters, methods were presented to make use of the information of experimental points beyond this limit, and several schemes were proposed to extrapolate small laboratory specimen resistance curves to large amounts of crack extension, using J_M , J_D , or other parameters [1.2].

Although the progress made has been significant, and understanding has been gained on how to represent the R curve [1.2-1.6], there are still several very important points that need to be addressed before the method can be safely applied.

Among the most important ones, is the need to extend this whole methodology to include cases involving three dimensions (3D): it is essential to know how specimen

thickness, constraint, and the possible dependence of the fracture mechanism on specimen thickness may affect the fracture resistance.

Ultimately, this knowledge gained from "2D" planar specimens should be used to explain and predict the behavior of real 3D defects found in structures, e.g., surface or embedded cracks.

1.3 The Leak Before Burst (LBB) Criterion

Pressure vessels containing surface flaws are often required to comply with the so-called LBB criterion. LBB is understood as the condition where, upon application of a load, an existing flaw is assumed to grow through the wall of a pressure vessel in a prescribed fashion, causing leakage before the pressure vessel bursts.

Pressure vessels of interest to NASA must comply to MIL-STD-1522A Standard General Requirements for Safe Design and Operation of Pressurized Missile and Space Systems. This document requires that: (1) the aspect ration, $A.R. = a/2c$ (crack depth to total width ratio) needs to be in a range from 0.05 and 0.5, and (2) LBB will occur if

$$K_{Ic} / \sigma_{\varphi} > 2\alpha B^{0.5} \quad \text{with } \alpha \sigma_{\varphi} < \sigma_{ys} \text{ and } \alpha > 1. \quad (1.1)$$

The rationale behind this expression is that the initial semi-elliptical flaw will grow in a self-similar manner, i.e., keeping A.R. = $a/2c$ constant until the crack depth a is exactly equal to the thickness B , as shown in Figure 1.1. At that time, it is considered that the flaw becomes a through crack with a total length of $2c$, with $2c = B/(A.R.)_0$, where the subscript 'o' is used to designate the initial state. Finally, to prevent the crack from running unstably in the longitudinal direction, i.e., bursting, the applied K given in equation 1.1 is required to be below the toughness K_{IC} associated with this final flaw configuration.

$$K_{app} = \sigma_{op} \sqrt{\pi c} \quad (1.2)$$

The MIL-Standard is inadequate for use with modern materials and designs because: (1) the above equation only holds for an aspect ratio A.R. = 0.5, (2) the flaw shape is considered to always remain elliptical with constant $a/2c$, and (3) the whole analysis is based on LEFM concepts.

On the other hand, for the real materials, thicknesses, and typical flaws of interest, the situation is markedly different from the one assumed, above. A growing crack, shown schematically in figure 1.2, is marked with the numbers 1, 2, and 3 to suggest the evolving shape that is observed. Cracks do not grow in an elliptical self-similar

manner, but rather in a very complex shape, with a dimension in the direction parallel to the surface that is longer in the interior than on the surface. Moreover there is no guarantee that this dimension can be conservatively estimated by taking the original $(2c/a)_0$ and multiplying by B.

1.4 This Project

The EPFM Methodology has evolved significantly in the last several years. Nevertheless, some of these concepts need to be extended further before the whole methodology can be safely applied to structural parts. Specifically, there is a need to include the effect of constraint in the characterization of material resistance to crack growth and also to extend these methods to the case of 3D defects.

As a consequence, this project was started as a 36 month research program with the general objective of developing an elastic plastic fracture mechanics methodology to assess the structural reliability of pressure vessels and other parts of interest to NASA which may contain flaws.

The project is divided into three tasks that deal with (1) constraint and thickness effects, (2) three-dimensional cracks, and (3) the Leak-Before-Burst (LBB) criterion.

Task 1. Constraint and Thickness Effects

This task includes the study of the problem of constraint and thickness effects observable in the fracture process, for different specimen sizes and geometries and for materials of interest.

Specifically, the following subtasks will be performed:

- a) The large body of available data from centers around the World will be gathered to study this effect in specimens of different size and geometry.
- b) Resistance to crack growth tests will be conducted using specimens of different size and geometry, on at least one material of interest. The material will be provided by NASA; Georgia Tech will machine the lab specimens.
- c) Characterization of fracture surfaces to determine mechanisms of fracture, and typical surface dimensions will be performed using modern quantitative metallographic techniques.

- d) Using the information obtained, models will be developed to describe the effect of constraint on the growth of cracks under elastic plastic conditions.

Task 2. Three Dimensional Cracks

The problem of applicability of EPFM concepts to 3D crack problems, in materials of interest, will be studied in this task.

Specifically, the following subtasks will be performed:

- a) Plates containing surface cracks with different initial crack aspect ratios and relative crack-to-plate geometry will be tested. The evolution of the crack shape (planar) and the crack surface displacement with loading will be determined.
- b) Analytical and numerical efforts will be devoted to determine values of J and constraint along the crack front.
- c) The models and information obtained from Task 1 will be used here to predict the behavior of these 3D cracks.
- d) Predictions and experimental results will be compared and, if necessary, refinement of the models will be made.

Task 3. Leak Before Burst (LBB) Criterion

The body of information obtained in the previous tasks will be organized in the spirit of the current LBB criterion into a Methodology format for the assessment of the structural integrity of parts containing defects.

1.5 This Report

This report covers the activities of the period March 1994 through August 1994. In this period, full advantage was taken from the experience and knowledge gained in previous projects [1.6-1.9]. In particular, some efforts were devoted in this project to complete and extend previously obtained results.

In Chapter 2, experimental efforts to characterize three dimensional aspects of fracture present in "two dimensional", or planar configuration specimens have been continued. Chapter 2 specifically contains the discussion associated with the determination of, and use of, crack face separation data.

In Chapter 3, the results of the fracture resistance testing for a variety of specimen configurations (J_{MR} -curve format) is presented. The discussion presents the bases for like constraint for two materials of interest to NASA-MSFC

(in particular, 6061-T651 aluminum alloy and IN718-STA1 nickel-base super alloy were characterized) in terms of the ligament dimensions, and compares these bases to the resulting J_M R-curves.

1.6 References for Chapter 1

- [1.1] Ernst, H. A., "Material Resistance and Instability beyond J-Controlled Crack Growth", *ASTM STP 803*, American Society for Testing and Materials, 1983.
- [1.2] Ernst, H. A. and Pollitz, E. T., "Fracture Toughness from Existing Surveillance Data", EPRI RP-2975-10, Preliminary Final Report, December 1988.
- [1.3] Landes, J. D., McCabe, D. E., and Ernst, H. A., "Elastic Plastic Methodology to Establish R-Curves and Instability Criteria", *EPRI Report RP-1238-2*, August 1982.
- [1.4] Kumar, V., German, M. D., and Shih, C. F., "An Engineering Approach for Elastic Plastic Fracture Analysis", *EPRI NP-1931*, July 1981.
- [1.5] Roos, E., Eisele, U., Silcher, H., and Spaeth, F., "The Influence of the Material Toughness and the State of Stress on Fracture of Large Scale Specimens", *Nuclear Engineering and Design* 102 (1987), Pp. 439-49.
- [1.6] Hiser, A., "Results of Testing A302", private communications, January 1988.
- [1.7] McCabe, D. E., and Ernst, H. A., "Predictive Methodology for Integrity of Tank Welds with Crack-like Defects:", *MEA Report*, November 1989.
- [1.8] Ernst, H. A., and Lambert, D. M., "Three Dimensional Aspects of Elastic Plastic Crack Growth", *NASA GSRP Grant, NGT-50641*.
- [1.9] Boatwright, D.W., *An Elastic-Plastic Fracture Mechanics Analysis of Semi-Elliptical Surface Crack Growth*, Master's Thesis, Georgia Institute of Technology, April 1993.
- [1.10] Curtin, W.J., *An Investigation of a Two Parameter Elastic-Plastic Fracture Mechanics Methodology*, Master's Thesis, Georgia Institute of Technology, June 1993.

1.7 Figures for Chapter 1

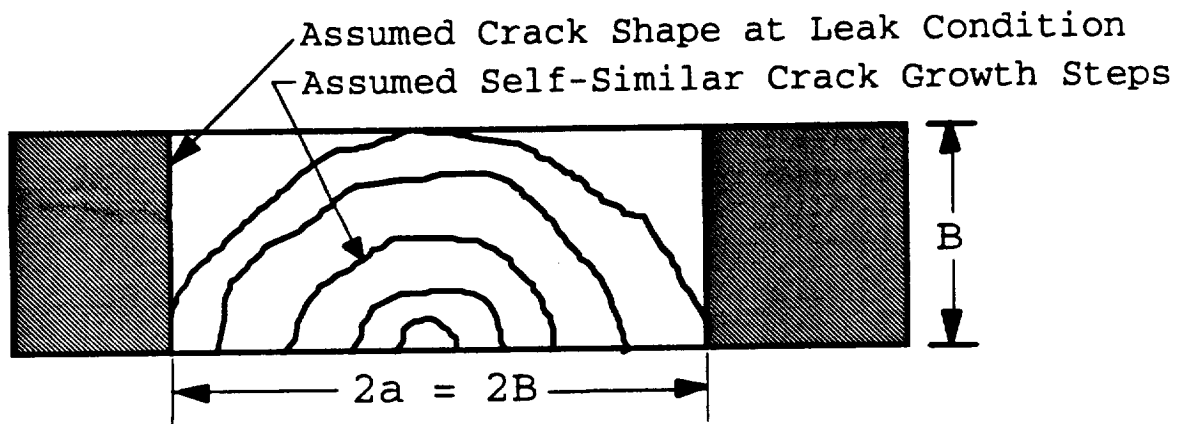


Figure 1.1 Simple Leak Criterion

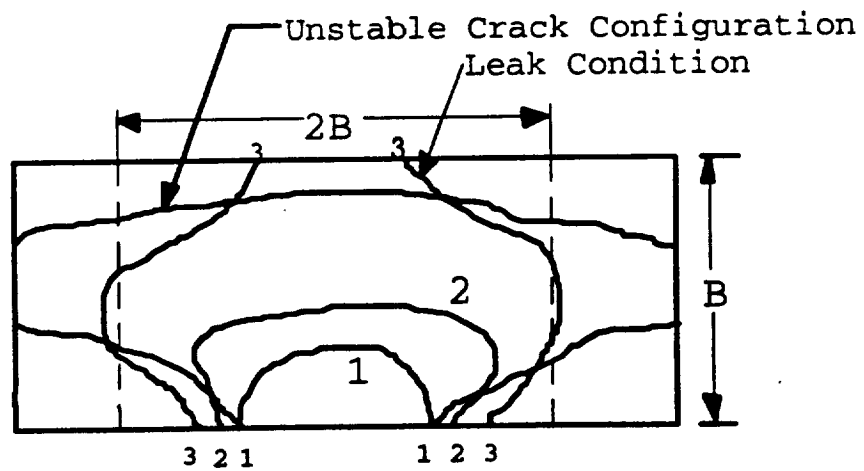


Figure 1.2: Actual Growth of a Part-Through Crack

CHAPTER II

EFFORTS TO CHARACTERIZE THREE-DIMENSIONAL EFFECTS OBSERVABLE IN TWO DIMENSIONAL FRACTURE SPECIMENS.

by D. Lambert and H. Ernst

2.1 Introduction

The underlying purpose of this research is to develop a methodology which would allow the characterization of three-dimensional (3D) effects in fracture. This characterization should include:

- a) elastic plastic fracture behavior
- b) geometric effects arising from crack front curvatures (curvatures are present, for example, with surface cracks),
- c) geometric effects related to thickness and ligament length (the gross sizing details that affect the three-dimensionality of the state of stress at the crack tip), and
- d) loading geometry effects (including three-dimensionality of the far field stress arising from the character of applied loads, and,

especially the gradient of the far-field stress arising from differing ratios of bending-to-tension).

Two-dimensional (2D) or planar specimens have been observed to generate different fracture resistance curves when different thicknesses are tested. Specifically discussed here are J_M R curves that use the J-modified parameter as developed by Ernst [2.1 and 2.2]. Different configurations have been shown to support a differing degree of triaxiality of the stress field in the vicinity of the crack front, where the fracture process is occurring. The degree of stress field triaxiality that is exhibited is referred to as the *constraint*. The J_M R curves are a result of the different, averaged constraint in each specimen. Even though the configurations are considered to be planar, curvatures can develop in crack fronts that result from fracture in the presence of a gradient of the constraint within the specimen. Thus, the complexities that occur in the most general cases of fracture appear in the simplest cases of planar specimens. Ultimately, to evaluate fracture resistance retaining a planar analogy requires that the crack front fall within specific limits of straightness.

Since, 3D stress fields are present in planar configurations, an effort to map the crack face separation profiles of a variety of geometries as a function of the

position within the cross-section has been proposed. The crack tip opening displacement (CTOD) is a linear function of the J-integral [2.3]. Profiling represents an extension of that functional relationship.

One goal of the overall research program is to test a wide variety of planar specimens, varying the thickness and length of the initial remaining ligament, as well as the bending-to-tension ratio due to the nature of the applied load to produce significant changes in fracture behavior. The results will be compared using the ligament dimensions as variables. Ultimately, the approach is expected to produce parameters and fracture behavior that can be generalized to the 3D cases that are of the most interest.

2.2 Introduction to Profiling

The displacement of the faces of a crack are a function of the loading and of the position. Using a two dimensional analogy, the displacement of a point along a crack face within an elastic body was given by Tada, et al [2.4]:

$$v_{cl} = \frac{4\sqrt{2}}{E'\sqrt{\pi}} K \sqrt{r} \quad (2.1)$$

Here, v_{el} is the elastic displacement in the loading direction at position r , measured from the crack tip to the point in question, E' is the equivalent modulus ($E'=E$ for plane stress, $E'=E/(1-\nu^2)$ for plane strain, E is Young's Modulus, and ν is Poisson's ratio). The loading is specified in the presence of a flaw by K , the stress intensity parameter. This displacement relationship has a square-root of r form.

Hutchinson [2.5] and Rice and Rosengren [2.6] developed a similar form for plastic response that follows Ramberg-Osgood deformation characteristics, i.e.:

$$\frac{\epsilon}{\epsilon_0} = \alpha \left(\frac{\sigma}{\sigma_0} \right)^n \quad (2.2)$$

In this equation, ϵ and σ are the equivalent strain and stress and ϵ_0 , σ_0 and n are material constants. The form of the plastic displacement is, as follows:

$$v_{pl} = k \cdot J_{pl}^{1/n} r^{1/n} \quad (2.3)$$

This equation is written for a non-growing crack, and v_{pl} is the displacement of the body, assuming Ramberg-Osgood type deformation, and k includes the functionality with regards

to the constraint, i.e., plane stress or plane strain condition. Looking at the equations (2.1) and (2.3), the constraint appears in the coefficient E' for the linear elastic case and in the coefficient k for the plastic case. Thus, the separation at various points through the ligament thickness could be expected to reflect that difference in constraint that arises with the depth into the thickness. It may also provide a measure of that constraint.

Since the development above is for a non-growing crack situation, differences that occur between the theoretical elastic plus plastic displacements and the displacement profile of an actual growing crack near the crack tip might provide a fracture criterion on that local level.

2.3 Profiling Matrix and Details

One objective in the research was to characterize the degree of separation between the mating surfaces of cracks. This separation profile is a function of the level of J and of the position within the ligament. In this case the position would include the distance from the load-line, x , in the direction of crack growth, and the depth beneath the surface in the thickness direction, z .

The primary effort in the past six months has been to analyze the crack face separation data of selected

specimens. The specimen identities and the corresponding configurations appear in Table 2.1, at the end of the chapter. Data was generated for a total of six compact tension (CT) specimens and three center-crack tension (CCT) specimens. The CCT configuration produces two crack profiles per specimen, and thus the total number of crack fronts observed is thirteen. Profiles were made of the AL6061-T651 only, because the IN718-STAl material has proven too hard to polish in the same fashion as the aluminum: epoxy infused into the gap of the crack was effective in producing a well-defined crack profile for the aluminum, but the profiles of the nickel were rounded and poorly-defined. Until the techniques have been modified to overcome the rounding, the profiling was suspended for the nickel.

After mounting the specimens in epoxy, the exposed surface was polished to provide a surface profile. After recording the profile, 0.025- to 0.035-inches was removed by grinding and polishing to produce the next profile to be recorded. This was continued for each specimen into the center of the cross-section.

2.4 Profiling Results

The crack tip opening displacement, δ_5 , was shown to be proportional to J or J_M by Hellmann and Schwalbe [2.7] and

Ernst, et al [2.8], and is used as a fracture parameter. The crack grows away from the location where δ_5 is measured, and the measurement is expected to eventually lose sensitivity. It was thought that the shape of the loaded crack might provide a useful modification of the δ_5 parameter, since the measurement location is being continuously updated as the crack grows. This section presents the results of efforts to establish the shape of the crack cavities of the compact tension and center-cracked tension specimens. The profiles are the "xy" plots of the crack shapes that were exposed by sectioning at different levels through the thickness. The results of the profiling will be given here.

The information shown herein is organized as follows:

- (1) observations of crack profiles through-the-thickness,
- (2) comparisons of crack face separation profiles of selected specimens,
- (3) stretch analysis and the correlations,
- and (4) initiation stretch, and (5) a discussion of the observations.

2.4.1 Crack Profiles

Although the individual profiles were not included, certain observations were made of their character, and these are summarized, below.

Figures 2.1 show the change of the crack shape as a function of the section depth for two specimens of different configurations. These figures show the shapes of the cracks at each of the section depths. Cross-sections were taken at each 0.025- to 0.030-inches starting at the specimen surfaces and continuing into their center planes. The fraction of depth below the surface is indicated by $Z \equiv 2z/B$ with $Z = 0$ at the surface and $Z = 1$ at the center plane. The vertical direction is the loading direction, and the horizontal direction is the direction of crack growth, with dimension referenced to the load line. The initial flaw location is indicated by " a_0 ". In figure 2.1a, the specimen is a CT specimen of thickness $B = .85$ -inches (specimen #C9, CT, $W = 2$ -inches, $B = 0.85$ -inches, $a/W = .5$). At the surface, the crack profile is sharply angled beyond the fatigue precrack. This angled crack shape is associated with shear (note that the two axes of the figures are not of equal magnification, thus the angle shown is not the true angle). For progressively deeper sections, the profiles become progressively straighter and longer.

Figure 2.1b is a similar development to figure 2.1a. In this case, the specimen is identical except for the thickness of 0.25-inches (specimen #51, CT, $W = 2$ -inches, $B = 0.25$ -inches, $a/W = 0.5$). This set of crack profiles again shows the same angled character at the surface and the

tendency toward straightness as the center section is approached.

2.4.2 Crack Face Displacement Profiles

An evaluation of the "calibration" value of the crack face displacement was computed as the sum of the elastic displacement plus an estimate of the plastic displacement. This total calibration displacement is a fitted function that agrees with the fatigue precrack region. The best fit to the precrack region appeared when the calibration was fitted using the length of the crack at the deepest point and had a form, as follows:

$$\delta_{fit}(r) = \frac{4K}{E'} \sqrt{\frac{2r_{sh}}{\pi}} + C_{pl} r_{sh}^q \quad (2.4)$$

In this equation, the calibration displacement is $\delta_{fit}(r)$, K is the average stress intensity factor, E' is the effective modulus, and r_{sh} is the position referenced to the deepest point of the crack front in the whole cross-section. C_{pl} and q are constants fitted to the precrack region. This calibration displacement was used to determine the *stretch*, discussed below. The stretch is calculated as the difference between the fracture profile and the calibration value.

Figures 2.2 - 2.4 show sets of the crack displacement profiles for five specimens. The precrack region has been omitted in the figures. Figure 2.2 presents one set of crack face displacement data for the entire cross-section of a typical specimen from surface to center. In this case, the specimen (#81, CT, $W = 2$ -inches, $B = 0.5$ -inches, $a/W = 0.75$) is the same as the two earlier specimens, except for having a longer initial crack length and an intermediate thickness. The horizontal axis is the crack extension from the initial average crack tip location. The initial crack tip is at the zero location on the horizontal and at the beginning of the test, the displacement was zero on the vertical. As the load was applied, the initial crack tip blunts upwards and eventually, the crack begins to grow to the right. At zero crack extension (left side of the graph) is the displacement associated with the tip of the fatigue precrack at the final position of the test. The crack has grown to the right while the points to the left of the evolving crack tip have displaced upwards. The surface cross-section plots (lowest plots in the figure) show a substantial stretching or blunting before the crack begins to grow. This is seen as a vertical excursion (stretch) in the displacement profiles with no significant horizontal excursion (crack extension). For example, the blunting of one of the surface plots is the segment labelled "AB" in

figure 2.2. For successively deeper sections, the stretch is progressively less, while in the cross-section the crack is progressively longer. At the center of the specimen (top plots in the figure), no discrete stretch zone is obvious. The data presented in figure 2.2 shows substantial noise, and so the plots have been filtered by a simple averaging technique to remove some of the noise without grossly affecting the shape of the displacement profiles.

Each of the graphs in figures 2.2 - 2.4 show all plots associated with one of the specimens. Following the curves from the top-left to the bottom-right, once the initial stretching has occurred, all of the profiles have roughly the same shape, i.e., all of the displacement profiles have the same displacement at the location of the initial crack tip (crack extension of zero), and eventually, they develop approximately the same slope. The difference is that the surface profiles first stretched and then began to fracture, while those beneath the surface stretched less and the crack has grown longer. It should be noted that a few of the surface profiles may appear identical. This is also true of some of the center profiles. A set of "transition profiles" can be seen that blends smoothly from the stretch-and-fracture behavior of the surface to that of the center. Figures 2.3 show two identical specimens from a multi-specimen test subjected to two different input displacements

and exhibiting intermediate and long crack growth (CT, $B = 1/2$ -inch, $a/W = 0.5$, intermediate growth: #84, long growth: #E2). For specimen #84, the surface displacements seem to be developing still, although the profiles are taking on the character of the early part of the profiles of specimen #E2.

The specific behaviors observed in figures 2.2 - 2.4 were separated onto figures 2.5 - 2.7 to better illustrate certain observations. Figures 2.5 show the first three surface profiles for two specimens (#C9, CT, $B = 0.85$ -inches, $a/W = 0.5$, and #D6, CCT, $B = 1/2$ -inches, $a/W = 0.5$). In each graph, the data plotted together are quite similar. The $Z \equiv 2z/B = 0$ plots are actually below the adjacent near-surface plots, but are quite similar. The crack has been grown to such a great length and substantial tunnelling has occurred, this is thought to be a secondary behavior arising from the thin surface section remaining once the center-plane crack has developed significantly. Figures 2.6 show that the center profiles for the three specimens stabilized to the same length and shape. Figures 2.7 show the transition profiles of one CT and one CCT specimen. In each case, if surface or center profiles showed the identical behavior, one of these was included for reference to the transition region, and thus the full range of profiles is represented. The profiles are taken (generally) at every .025 to .030 inches, and in figure 2.7a the profiles seem to

be equally spaced. This is not so obvious in the CCT specimen profiles in figure 2.7b. The author suspects that the behavior of the CCT profiles (figure 2.7b) would be best described as a surface effect that occurs for all but the inner-most sections.

The similarities and transition characteristics described in the presentation above will be discussed in more specific detail below.

2.4.3 Stretch Analysis

The deviation of the separation profiles from the calibration profiles is a result of the growth of the crack from the initial position to the final position as the load-line displacement is being applied. For surface sections, the difference is quite pronounced, but for center sections, the deviation is insignificant. One point to be raised here is that the anticipated calibration profiles were expected to be parabolic, but it was seen that the fit was concave-upwards in many cases. The plastic component of the calibration function, the second term in equation 2.4 has an exponent q of less than unity. This exponent is shown in the EPRI handbook [2.9] as $q = 1/(n+1)$, which for this material is $q = 0.048$. Clearly, this is not the case. The fit using $q = 0.048$ does not fit the precrack region well. It was finally decided that the specimen configurations were

such that the single-term calibration was not accurate in the precrack region, and perhaps some beam deflection effect was being pronounced in the profiles. In support of this, two thoughts are offered: (a) the fit functions used do seem to fit the fatigue precrack region well with few exceptions, and (b) in the case of the center plots of the specimen #C9 (CT, $W = 2$ -inches, $B = 0.85$ -inches, $a/W = 0.5$), the concave upwards curve yields a similar shape to that of the data all the way to the tip of the crack. The use of $q \approx 0.048$ would require that the apparent crack length be shorter than the final crack. Further investigation into the proposed beam deflection effect or to find the appropriate calibration function might be warranted, however the results presented here are consistent and physically reasonable.

The deviation between the calibration profile and the data is referred to as *stretch*. The next set of figures, 2.8 - 2.12, show the stretch developed by the specimens at different section-depths. Figures 2.8 show surface stretch plots for four of the specimens. First, some of the stretch occurs devoid of crack growth, and then crack extension begins. Once the crack begins to extend at the section, it appears that the stretch may continue to increase, and this is true of all but the stretch profiles of the CCT specimen (figure 2.8d). The CCT surface stretch profiles, seem

horizontal. This increase may be a result of the use of improper calibration functions, although some inclination is expected. Otherwise, unstable fracture behavior would result.

Moving to the center stretch profiles in figure 2.9, the initial stretch observed at the surface prior to crack extension is gone. The center stretch figure 2.9a and 2.9b are flat, suggesting that the stretch is not present, but only crack extension plus the presence of the calibration displacement.

The transition from the surface stretch profiles to those of the center are shown in figure 2.10, these show the change of stretch characteristics as a function of the section depth for each specimen. The results presented in figure 2.10b should be taken very qualitatively, because in the middle sections of this recorded transition, the calibration profiles were found to fit best for the concave upwards calibration, thus these stretch profiles should not be compared, except at best to produce a trend.

Figures 2.11 show all of the stretch profiles for two of the specimens. In figure 2.11a, the intermediate crack growth specimen (#84, CT, $B = 1/2$ -inch, $a/W = 0.5$) is presented. The figure shows a surface-to-center transition except for the two centermost sections, perhaps. No summary figure has been provided, but the behavior is identical to

that of the early growth portion of the long crack growth specimen (#E2, CT, $B = 1/2$ -inch, $a/W = 0.5$).

Figure 2.11b shows all of the stretch profiles for a thin specimen (specimen #51, CT, $W = 2$ -inches, $B = 0.25$ -inches, $a/W = 0.5$). Only the center-most two profiles appear to be similar. The observed stretch profile behavior is better characterized by a continuous transition from surface behavior to center behavior with no region of similar stretch characteristics.

Figure 2.12 was included to show a comparison of the surface stretch characteristics of all of the specimens profiled. In this case, three behaviors appear, and these align by the different R_L ratios of the specimens profiled. The uppermost curves are of $R_L \equiv b_0/B = 2$, and both are from the same specimen. These curves show an increasing slope after the initial stretch phenomenon. The $R_L = 1$ surface sections produce a second, shallower slope, and six curves are present from two different specimens. The $R_L = 4$ and the CCT surface stretch plots possess a surface stretch character that appears to be similar and is horizontal after the initiation stretch. For all of the specimens shown, the initiation stretch is approximately the same. The slope following initiation could be representative of different stretch-versus-crack extension characteristics for the

different configurations, but is more likely due to the choice of an inaccurate calibration function.

No graphs of the center stretch profiles have been included, because it is thought that these would be misleading. The behavior can be summarized, as follows.

- a) The center stretch profiles show negligible initial stretch behavior before the crack begins to grow.
- b) Once the crack begins to grow in a given center cross-section, the stretch continues to evolve as the crack grows for the $R_L = 2$ and the CCT specimens (figures 2.9c and 2.9d), while for the $R_L = 1$ and the $R_L = 4$ specimens it appears that the the stretch may increase only slightly as the crack extends (figures 2.9a, 2.9b, and 2.12). Again, only a qualitative evaluation is recommended in the absence of verified, correct calibration functions. Some quantitative analysis will be performed in the next chapter, however the results should be considered to have a low level of confidence.

2.5: Initiation Stretch

When a crack extends into a structural ligament, the newly created surfaces are displaced from each other. The

displacement has been found to be related to the J-integral [e.g., 2.8].

$$\delta = d_n \frac{J}{\sigma_{ys}} \quad (2.5)$$

Here, δ is the crack tip-opening displacement, J is the value of the applied J-integral, σ_{ys} is the yield strength, and d_n is a parameter, approximately equal to unity, that accounts for the differences in constraint. The observation of the relationship between δ and J has lead to the idea that a measured displacement might be used to describe fracture behavior. Various definitions for δ can be offered, e.g., Hellmann, et al, [2.7] defined δ_5 , the displacement of a 5-millimeter gage length positioned at the original crack tip. This measurement was taken between two gage points, although the crack extended to positions increasingly more remote from the measuring points. The profiling effort in this investigation extended the measurement methodology to the tip of the current crack position. A calibration displacement was approximated and the remainder of the total crack face displacement was δ_{st} , the stretch. This has been fit to a form as follows:

$$(\delta_a - \delta_{cal}) = C_a (\chi)^p \quad (2.6)$$

The values of δ_{ref} and C_{st} come from a linear regression analysis of δ_{st} versus $(\chi)^p$, with χ being the crack extension (the distance in the profile from the initial crack tip position to the final crack tip position, $\chi = a_f - a_0$). Whereas the value of C_{st} is somewhat intuitive, that of δ_{ref} is not obvious: the regression analysis produced better correlation with δ_{ref} than if the regression was forced through $\delta_{ref} = 0$. It will be noted that the exponent of χ is $p = 1/(n+1) = .0483 \approx 0$, and with values of $C_{st} \approx 0$, it is suggested that the value of δ_{ref} might best describe the initiation stretch for a given profile. The data for the various fit parameters follow in the tables below along with a discussion of anomalies, special treatment received, and implications of the outcome.

Several characteristics were observed in the profile fitting efforts that should be mentioned. First, although exceptions existed, the elastic and plastic displacement fits to the precrack region of the profiles produced relatively constant coefficients. For a given specimen, the coefficients were approximately the same for all of the profiles. One intended output to be extracted using the calibration displacement fit was the stretch. The resulting stretch traces were then fitted as a function of the local crack extension, $\chi \equiv a_f - a_0$, raised to a power of $p = .0483$. This corresponds to displacements associated

with power-law plasticity, however it should be noted that the stretch displacement is a deviation from the bulk material behavior, represented by the calibration displacement. The early part of the stretch curves seemed to be almost vertical, exhibiting blunting, and then the stretch became approximately constant. Thus, imposing the exponent of p seemed reasonable. The resulting coefficients from the linear fit of the stretch to χ raised to p appear in each table, above. Two behaviors were apparent: (1) the values of C_{st} were relatively constant for the surface profiles, and the center profiles were a different constant C_{st} , and (2) the values of δ_{ref} seemed to be increasingly negative for the progressively deeper profiles. The form of the fit of the stretch in this material gives

$$\delta_s = \delta_{ref} + C_s (\chi)^p \approx \delta_{ref} + \zeta C_s \equiv \delta_i \quad (2.7)$$

A factor of ζ has been inserted to produce the value of the second term in the middle expression in equation 2.7 at the knee of the curve. The approximation on the right in equation 2.7 is reasonable in the event that the exponent p is much less than unity (for AL6061-T651, $p = .0483$), producing relative insensitivity of δ_{st} with respect to χ above a nominal level of χ . The value of the sum, δ_i , appears in the right-most column in each table and is

monotonically increasing for most of the compact tension specimens, and is relatively constant for the center-crack tension specimens. Ultimately, two different thoughts arise from these observations: first, the ligament of the CCT specimens must be more uniformly deformed throughout the whole of the fracture process, only exhibiting a small initiation stretch. Second, at least for this material that approximates elastic-perfectly plastic behavior, the initiation stretch, δ_i , appears to be a function of s , the depth beneath the surface. A strict definition of s is necessary at this point. The first profile was taken at the root of the necked region formed on the side of the specimen. This was assigned a value of $z = 0$ inches. Because of the necking phenomenon, the $z = 0$ surface is somewhat below the original surface, and thus, s was defined as z plus the neck-root depth. Figure 2.13 shows δ_i , the initiation stretch, versus s for all of the profiles. The lines connect adjacent profiles in each specimen. The initiation stretch decreases as s increases, but the correlation between specimens is not as obvious.

Various forms were considered to establish the nature of the behavior of δ_i versus s , and clearly the best correlation was with a parameter $sB/b_0 \equiv \kappa$, and this correlation is plotted in figure 2.14. Several features visible in the figure must be discussed. δ_i increases from

the surface profile to some peak value and then decreases as κ increases further. With the exception of the surface behavior and the behavior of the data indicated with dashed lines, all of the behavior seems to be along the same curve within experimental error. No obvious explanation exists for the results of the CCT specimen in the figure. Figures 2.15 have been included to segregate certain behaviors observed. The surface profiles, the $R_L = 4$ data, and the CCT data points have been excluded from the data set in figure 2.15a. The initiation stretch data that remains in this figure shows a consistent trend. Figure 2.15b shows the surface points and includes all of the data from the two specimens with $R_L = 4$. The horizontal axis position is the location of the root of the neck expressed as κ . The curve of the surface plots appears to be almost vertical, except that the lowest data points do show an increase in κ from the other data. A possible explanation for the behaviors in the figures 2.15 is this: for each specimen, a surface zone exists, and as the depth below the surface increases, the surface effect makes a transformation into the uniform subsurface behavior that is shown in figure 2.15a. In the case of the two specimens with $R_L = 4$, the surface effect permeates the whole thickness, and the entire cross-section degenerates into a surface effect defined simply by the

calibration profile up to the point of initiation of crack growth.

The maxima of each δ_i -versus- s curve occurs on the "uniform subsurface" curve shown in figure 2.15a, and the maximum initiation stretch can be estimated by the median value of $\delta_i B/b_0 = .03 = \text{constant}$. The minimum value is zero.

The results suggest that given a method to evaluate the constraint along an arbitrary crack front, and the boundary conditions, the calibration displacement of each point could be determined, and an estimate of the stretch and crack growth characteristics of the point might be easily determined by comparing to the results of such a planar crack growth analysis as presented, above.

2.6 Conclusions and Recommendations

1. The profiling procedures used to generate the crack face separation throughout planar specimen cross-sections showed that the δ_5 -displacement, measured at the surface was the same as the displacements observed inside the cross-section.
2. The δ_5 -displacement that is a common throughout the specimen cross-section at the initial crack tip is developed in a different manner depending on the

depth into the thickness considered. The onset of crack extension was termed the initiation stretch, δ_i . The value of δ_i seemed to be a function of the depth beneath the surface, although an alternate functionality that included the ligament proportions and the depth beneath the surface was also suggested.

- a) At some depth, the stretch prior to initiation is negligible. This is thought to be the plane strain condition.
 - b) For all of the cross-sections, the crack angle was approximately constant through the cross-section after crack growth initiates.
3. The use of profiling techniques shows some promise in the characterization, and profiling or some nondestructive technique (NDT), such as computer tomography, might be employed for a different material, e.g., IN718-STA1, to compare with results of the AL6061-T651. The destructive nature of the profiling procedures is not expected to affect the results much, but NDT techniques would avoid the potential influences altogether.

2.7 References for Chapter 2

- [2.1] H. A. Ernst, "Material Resistance and Instability beyond J-Controlled Crack Growth", *Elastic Plastic Fracture: 2nd Symposium, Volume I--Inelastic Crack Analysis*, ASTM STP 803, Shih and Gudas, Ed., (1983), Pp. I-191-213.
- [2.2] Ernst, H. A., "Further Developments on the Modified J-Integral", ASTM STP 995, (1989), Pp. 306-19.
- [2.3] Rice, J. R., "A Path Independent Integral and the Approximate Analysis of Strain Concentration by Notches and Cracks", *Journal of Applied Mechanics, Transactions of the ASME*, June 1968.
- [2.4] Tada, H., Paris, P. C., and Irwin, G. R., *The Stress Analysis of Cracks Handbook*, Second Edition (1985), Del Research Corp., St. Louis, MO.
- [2.5] Hutchinson, J. W., "Plastic Stress and Strain Fields at the Crack Tip", *Journal of the Mechanics and Physics of Solids*, Vol. 16 (1968), Pp. 337-47.
- [2.6] Rice, J. R., and Rosengren, G. F., "Plane Strain Deformation Near a Crack Tip in a Power-Law Hardening Material", *Journal of the Mechanics and Physics of Solids*, Vol. 16 (1968), Pp. 1-12.
- [2.7] Hellman, D., and Schwalbe, K. H., "Geometry and Size Effects on JR- and δR -Curves Under Plane Stress Conditions", ASTM STP 833 (1984), pp. 577-605.
- [2.8] Ernst, H. A., Schwalbe, K. H., Hellman, D., and McCabe, D. E., "Modified J, J_M . Resistance Curves Under Plane Stress", *International Journal of Fracture*, Vol. 37 (1988), pp. 83-100.
- [2.9] *An Engineering Approach for Elastic-Plastic Fracture Analysis*, Electric Power Research Institute Report NP-1931, Research Project 1237-1, prepared by General Electric Company (July 1981).

2.8 Tables for Chapter 2

Table 2.1: Matrix of Specimens Profiled

(W, B, and b are in inches, a/W is nondimensional)

Spec	Config	W	B	b	a/W	Remarks	No of Profs
E2	1T-CT	2	1/2	1	.5	Baseline Specimen	8
81	1T-CT	2	1/2	.5	.75	Larger Init. a/W	8
51	1T-CT	2	1/4	1	.5	Thinner Section	5
C9	1T-CT	2	.85	1	.5	Thicker Section	13
82	1T-CT	2	1/2	1	.5	Multi-Specimen	8
84	1T-CT	2	1/2	1	.5	Multi-Specimen	8
08	1T-CT 20%SG	2	1/2	.8	.6	Side-Grooved	8
D6	CCT	1	1/2	.5	.5	Tension	2x8
55	CCT	1	1/8	.5	.5	Tension, Thin	2x3
B9	CCT	1	.85	.5	.5	Tension, Thick	2x9

Table 2.2: Fitting Constants for CT Profiles

Specimen 82: AL, 1T-CT, B=1/2 inch, a/W=.5, Short Crack Growth									
Profile	s	Δr_{sh}	f_{e1}	C_{n1}	q	δ_{ref}	C_{sr}	δ_i	Comments
8201	.01 2	-.216	1	.003	.99	X	X	X	
8202	.03 9	-.204	1	.002	-.05	X	X	X	m ≈ 0
8203	.06 4	-.192	1	.006	.87	X	X	X	
8204	.09 3	-.175	1	.007	.95	X	X	X	
8205	.12 5	-.137	1	.009	1.0	X	X	X	
8206	.17 6	-.080	1	.011	.96	X	X	X	
8207	.20 7	-.053	1	.006	.86	X	X	X	
8208	.23 8	0	1	.008	1.1	X	X	X	

Table 2.3: Fitting Constants for CT Profiles

Specimen 84: AL, 1T-CT, B=1/2 inch, a/W=.5, Intermediate Crack Growth									
Prof.	s	Δr_{sh}	f_{e1}	C_{n1}	q	δ_{ref}	C_{sr}	δ_i	Comments
8401	.022	-.237	1	.042	.58	-.14	.20	.039	C_{sr} large
8402	.050	-.222	1	.035	.71	-.07	.10	.026	
8403	.075	-.207	1	.034	.70	-.06	.09	.022	
8404	.108	-.163	1	.033	.67	-.09	.12	.021	
8405	.136	-.118	1	.035	.61	-.13	.16	.016	
8406	.168	-.074	1	.033	.65	-.11	.13	.010	
8407	.194	-.038	1	.034	.64	-.13	.15	.007	
8408	.210	0	1	.030	.62	-.02	.02	.004	C_{sr} small

Table 2.4: Fitting Constants for CT Profiles

Specimen E2: AL, 1T-CT, B=1/2 inch, a/W=.5, Long Crack Growth									
Profile	s	Δr_{sh}	f_{e1}	C_{n1}	q	δ_{ref}	C_{sr}	δ_i	Comments
E201	.020	-.160	1	.134	.83	-.16	.21	.029	C_{sr} small
E202	.045	-.325	1	.107	.95	-.24	.30	.031	
E203	.069	-.308	1	.111	1.0	-.30	.36	.024	
E204	.101	-.272	1	.114	1.2	-.34	.38	.012	
E205	.134	-.237	1	.114	1.1	-.26	.30	.013	
E206	.161	-.114	1	.114	1.1	-.36	.40	.002	
E207	.192	-.037	1	.112	1.1	-.24	.26	.001	C_{sr} small
E208	.223	0	1	.110	1.0	-.16	.18	.002	C_{sr} small

Table 2.5: Fitting Constants for CT Profiles

Specimen 81: AL, 1T-CT, B=1/2 inch, a/W=.75, Long Crack Growth									
Profile	s	Δr_{sh}	f_{p1}	C_{n1}	q	δ_{ref}	C_{sr}	δ_i	Comments
8101	.027	-.231	1	.105	1.2	-.15	.19	.022	
8102	.058	-.204	1	.114	1.1	-.13	.17	.024	
8103	.090	-.167	1	.114	1.1	-.12	.16	.019	
8104	.116	-.110	1	.116	1.1	-.05	.07	.014	
8105	.150	-.029	1	.104	.99	-.22	.26	.011	C_{sr} large
8106	.182	0	1	.122	1.2	-.03	.03	.002	
8107	.221	-.014	1	.117	1.1	-.02	.02	.003	
8108	.245	-.006	1	.107	1.0	-.02	.03	.003	

Table 2.6: Fitting Constants for CT Profiles

Specimen 51: AL, 1T-CT, B=1/4 inch, a/W=.5, Long Crack Growth									
Profile	s	Δr_{sh}	f_{p1}	C_{n1}	q	δ_{ref}	C_{sr}	δ_i	Comments
5101	.027	-.151	1	.061	.88	-.04	.06	.015	
5102	.058	-.117	1	.061	.86	-.04	.06	.011	
5103	.085	-.071	1	.061	.84	-.08	.10	.006	
5104	.115	0	1	.060	.81	-.04	.05	.004	
5105	.147	-.008	1	.060	.87	-.04	.04	.003	

Table 2.7: Fitting Constants for CT Profiles

Specimen C9: AL, 1T-CT, B=.85 inch, a/W=.5, Long Crack Growth									
Profile	s	Δr_{sh}	f_{p1}	C_{n1}	q	δ_{ref}	C_{sr}	δ_i	Comments
C901	.022	-.382	1	.058	.94	-.08	.12	.022	C_{sr} small
C902	.054	-.476	1	.038	1.6	-.13	.17	.023	
C903	.082	-.504	1	.033	1.6	-.13	.16	.021	
C904	.109	-.440	1	.037	1.4	-.18	.22	.017	C_{sr} large
C905	.150	0	1	.057	.69	-.07	.09	.010	
C906	.201	0	1	.046	1.0	-.04	.05	.006	
C907	.243	-.057	1	X	X	X	X	X	
C908	.285	0	1	.041	1.3	-.03	.03	.003	

C909	.341	-.005	1	.042	1.4	-.02	.02	.002	
C910	.390	0	1	.040	1.3	-.03	.03	.001	
C911	.424	-.019	1	.040	1.5	-.02	.03	.002	

Table 2.8: Fitting Constants for CCT Profiles

Specimen #55, AL, CCT, 2W=2 inch, B=.125 inch, a/W=.5									
Profile	s	Δr_{sh}	f_{e1}	C_{n1}	q	δ_{ref}	C_{sr}	δ_i	Comments
55A01	.010	0	1	.007	.08	-.04	.06	.013	
55A02	.038	0	1	.009	.14	-.06	.07	.011	
55A03	.063	0	1	.006	-.08	-.10	.12	.015	

Table 2.9: Fitting Constants for CCT Profiles

Specimen D6: AL, CCT, 2W=2 inch, B=1/2 inch, a/W=.5									
Profile	s	Δr_{sh}	f_{e1}	C_{n1}	q	δ_{ref}	C_{sr}	δ_i	Comments
D6A01	.019	0	0	.042	.41	.00	.02	.020	
D6A02	.052	0	0	.043	.39	.01	.01	.020	
D6A03	.083	0	0	.040	.28	-.01	.04	.022	
D6A04	.113	0	0	.032	.15	-.14	.17	.020	
D6A05	.140	0	0	.043	.36	-.02	.04	.014	
D6A06	.166	0	0	.032	.05	-.07	.11	.026	
D6A07	.204	0	0	.033	.15	-.08	.10	.013	
D6A08	.236	0	0	.030	.12	-.08	.10	.012	

Table 2.10: Fitting Constants for CCT Profiles

Specimen B9: AL, CCT, 2W=2 inch, B=.85 inch, a/W=.5									
Profile	s	Δr_{sh}	f_{e1}	C_{n1}	q	δ_{ref}	C_{sr}	δ_i	Comments
B9A01	.017	0	.5	.002	-.16	X	X	X	
B9A02	.050	0	.5	.003	.26	-.00	.01	.005	
B9A03	.084	0	.2	.007	.01	-.02	.04	.010	
B9A04	.155	0	.3	.006	.10	-.02	.02	.002	
B9A05	.196	0	.4	.006	.38	-.00	.00	0	
B9A06	.238	0	.3	.005	.16	-.00	.01	0	
B9A07	.295	0	.3	.006	.37	-.01	.01	X	
B9A08	.357	0	.4	.002	.14	-.01	.01	.001	
B9A09	.421	0	.3	.009	.77	-.01	.01	0	

2.9 Figures for Chapter 2

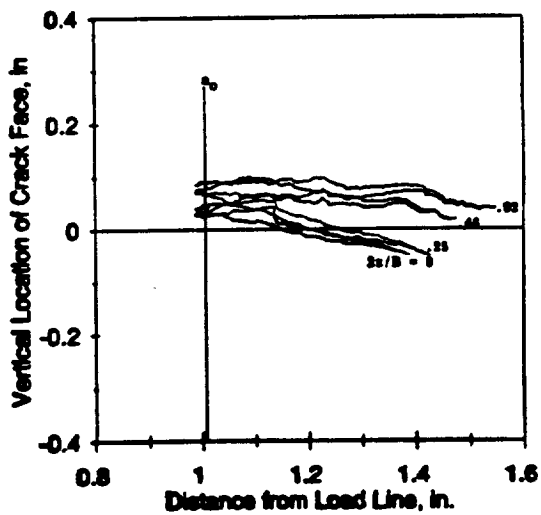
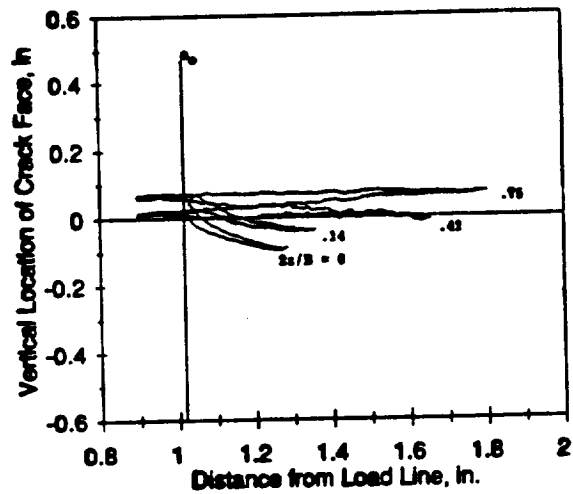


Figure 2.1: Typical cross-sections of cracked specimens, showing crack profiles from surface to center plane: (a) specimen #C9 (CT, $B = 0.85$ -inches, $a/W = 0.5$), and (b) specimen #51 (CT, $B = 1/4$ -inches, $a/W = 0.5$).

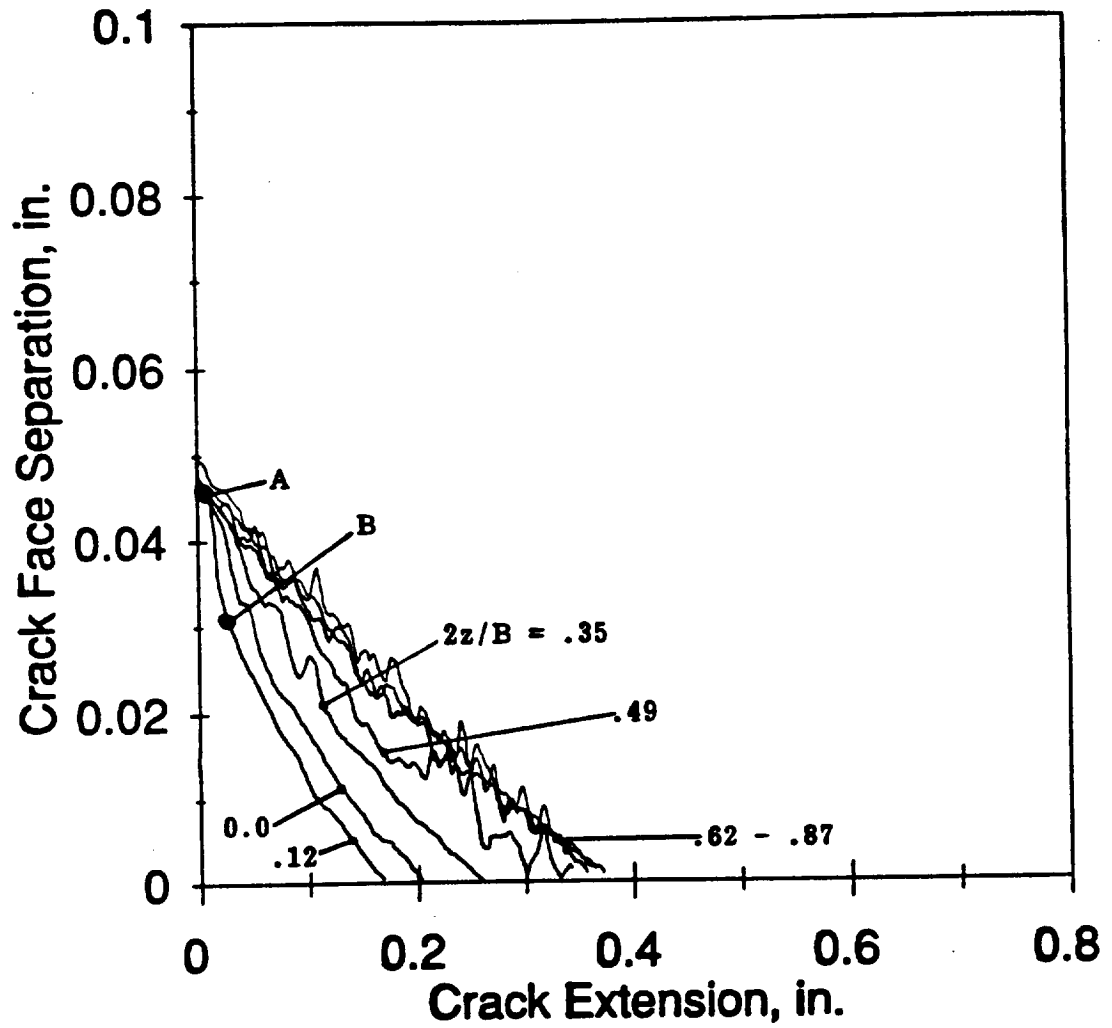


Figure 2.2: Crack face separation profiles for cross-sections from surface to center plane of specimen #81 (CT, $B = 1/2$ -inch, $a/W = 0.75$). Note: the normalized depth is $2z/B = 0$ at surface and $2z/B \approx 1$ at center.

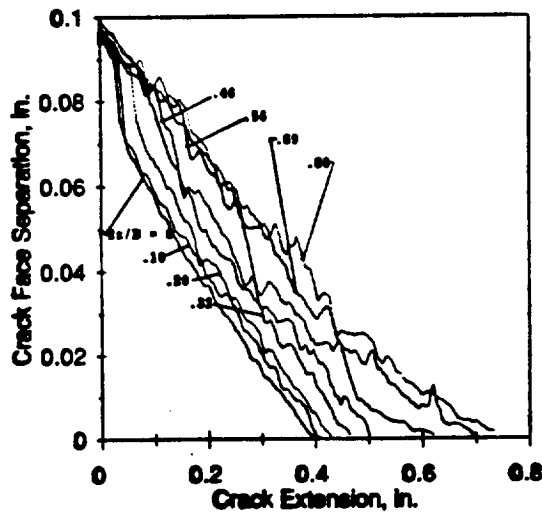
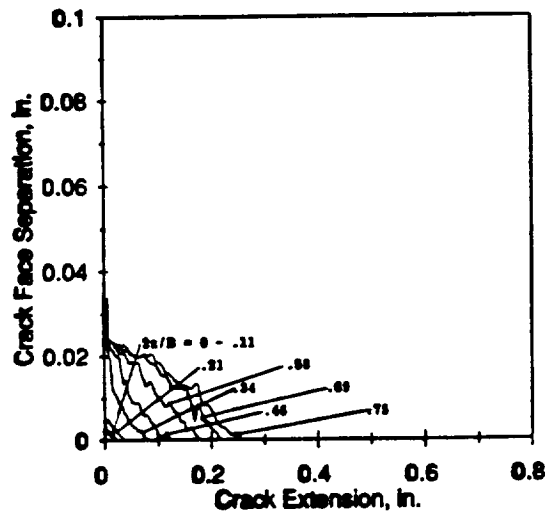


Figure 2.3: Crack face separation profiles for cross-sections from surface to center plane of two specimens from multiple-specimen test (CT, $B = 1/2$ -inch, $a/W = 0.5$): (a) intermediate growth, specimen #84, and (b) long growth, specimen #E2. Note: the normalized depth is $2z/B = 0$ at surface and $2z/B \approx 1$ at center.

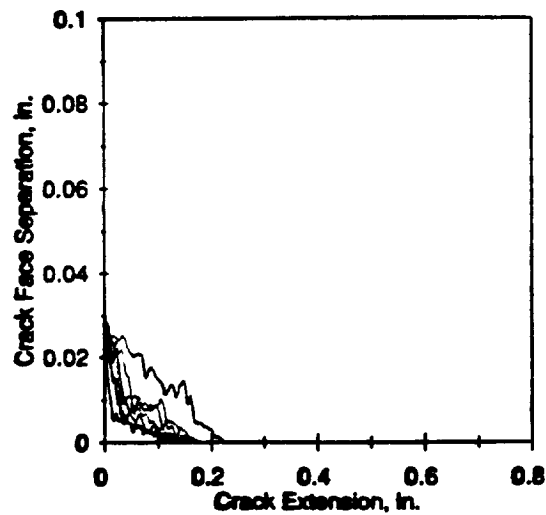
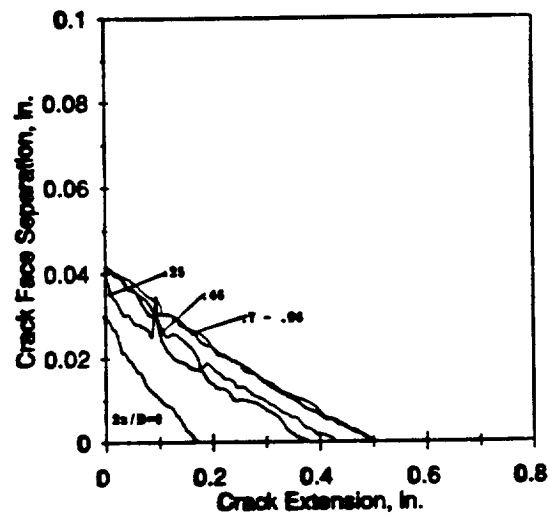


Figure 2.4: Crack face separation profiles for cross-sections from surface to center plane of two specimens of different configuration (a) specimen #51 (CT, $B = 1/4$ -inch, $a/W = 0.5$), and (b) specimen #D6 (CCT, $B = 1/2$ -inch, $a/W = 0.5$). Note: the normalized depth is $2z/B = 0$ at surface and $2z/B \approx 1$ at center.

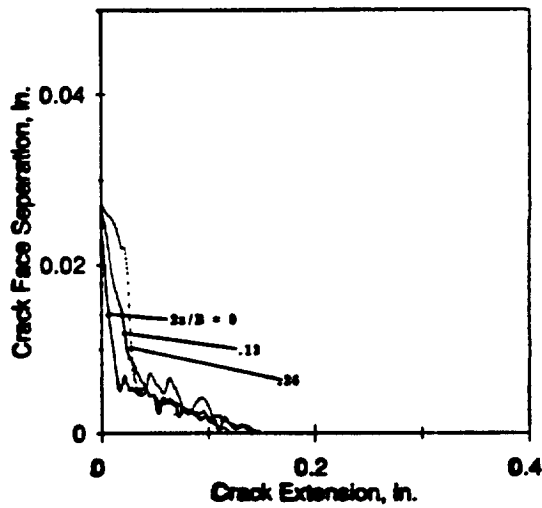
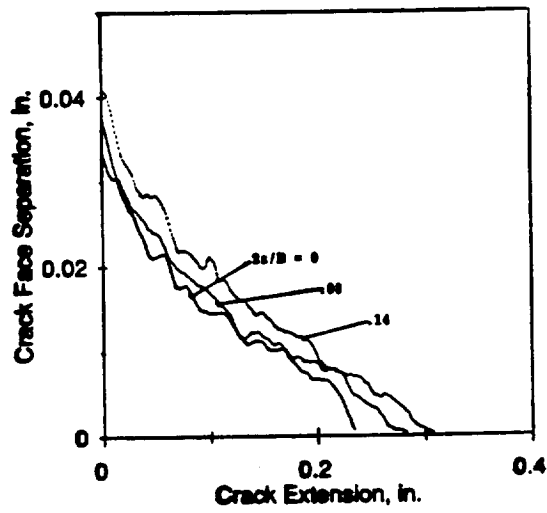


Figure 2.5: Crack face separation profiles for near-surface cross-sections of two specimens: (a) specimen #C9 (CT, $B = 0.85$ -inch, $a/W = 0.5$), and (b) specimen #D6 (CCT, $B = 1/2$ -inch, $a/W = 0.5$). Note: the normalized depth is $2z/B = 0$ at surface and $2z/B \approx 1$ at center.

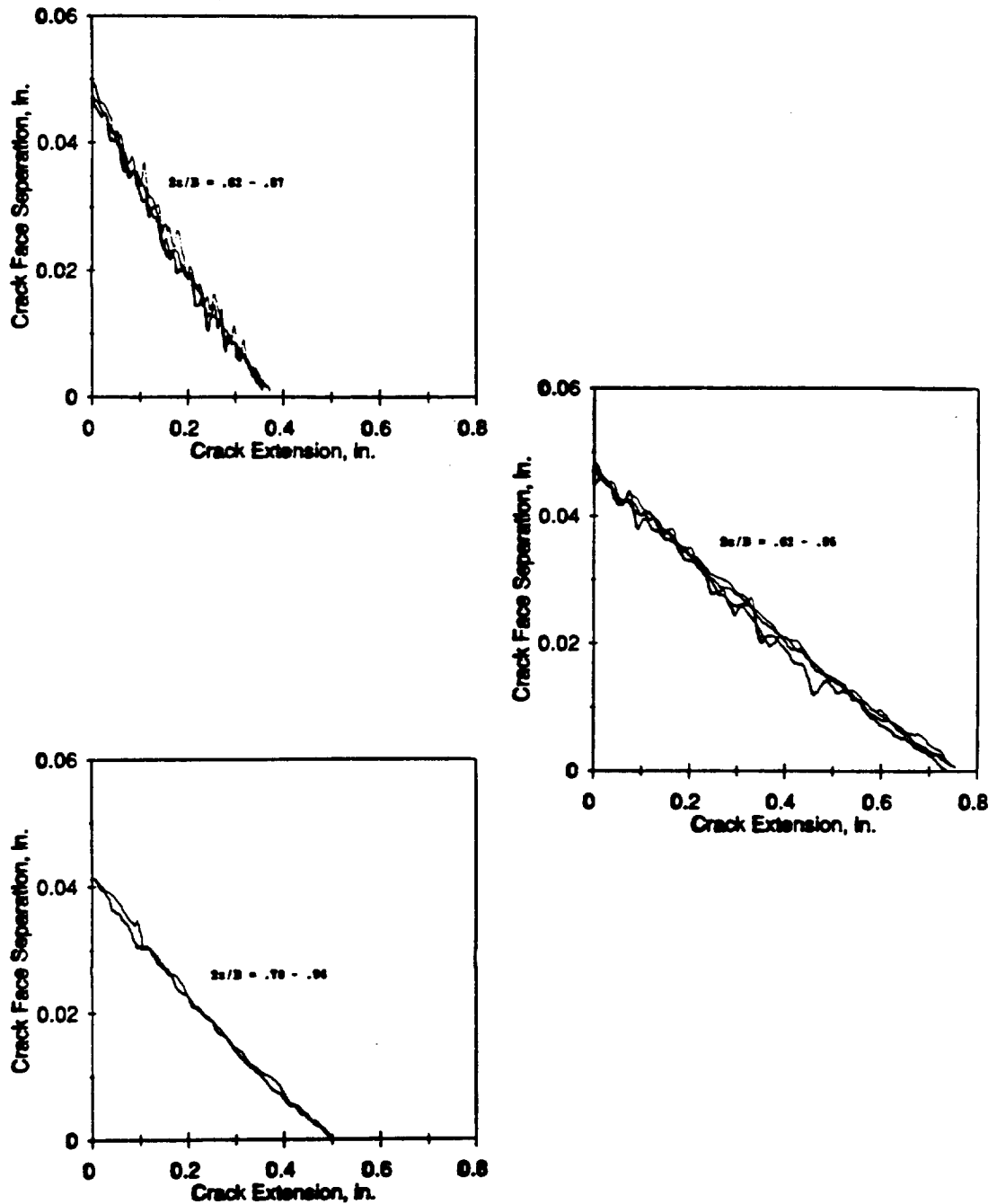


Figure 2.6: Crack face separation profiles for center plane cross-sections of three specimens: (a) specimen #81 (CT, $B = 1/2$ -inch, $a/W = 0.75$), (b) specimen #C9 (CT, $B = 0.85$ -inch, $a/W = 0.5$), and (c) specimen #51 (CT, $B = 1/4$ -inch, $a/W = 0.5$). Note: the normalized depth is $2z/B = 0$ at surface and $2z/B = 1$ at center.

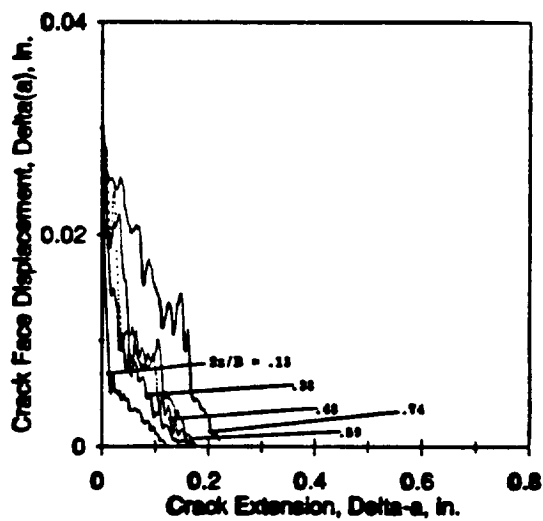
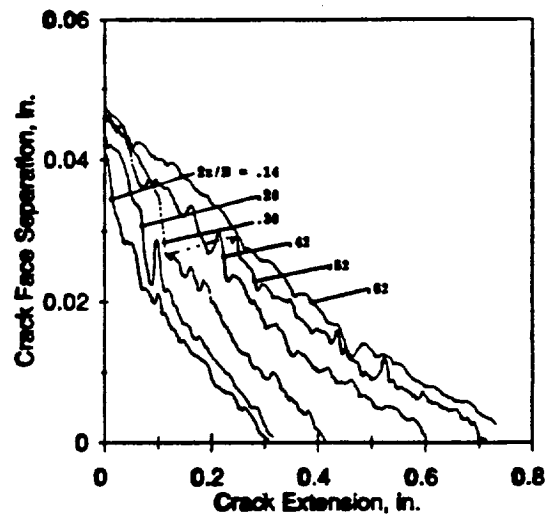


Figure 2.7: Crack face separation profiles of two specimens from surface to center plane: (a) specimen #C9 (CT, $B = 0.85$ -inch, $a/W = 0.5$), and (b) specimen #D6 (CCT, $B = 1/2$ -inch, $a/W = 0.5$). Note: the normalized depth is $2z/B = 0$ at surface and $2z/B \approx 1$ at center.

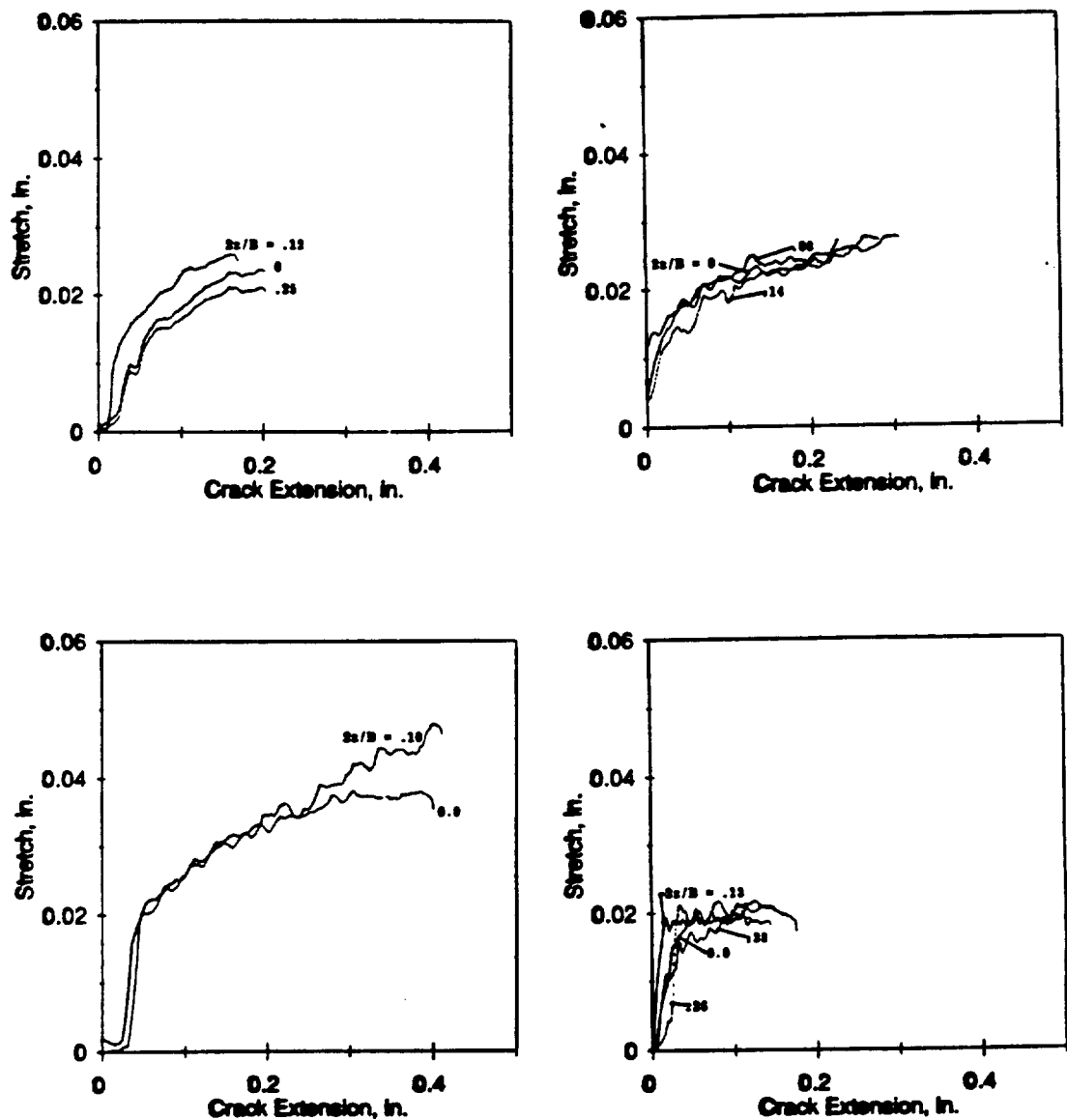


Figure 2.8: Stretch-versus-crack extension data for near-surface cross-sections of four specimens: (a) specimen #81 (CT, $B = 1/2$ -inch, $a/W = 0.75$), (b) specimen #C9 (CT, $B = 0.85$ -inch, $a/W = 0.5$), (c) specimen #E2 (CT, $B = 1/2$ -inch, $a/W = 0.5$), and (d) specimen #D6 (CCT, $B = 1/2$ -inch, $a/W = 0.5$). Note: the normalized depth is $2z/B = 0$ at surface and $2z/B = 1$ at center.

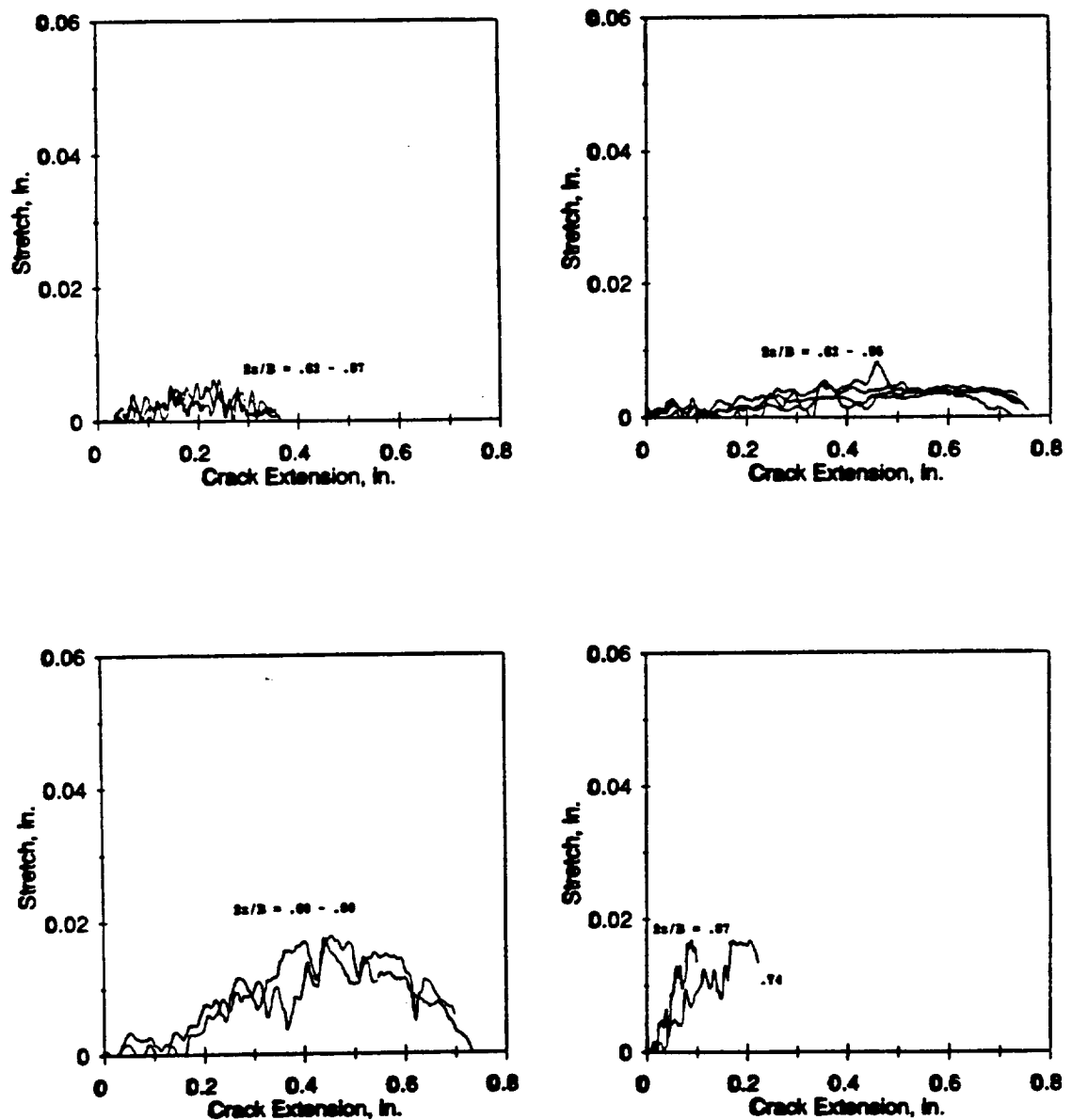


Figure 2.9: Stretch-versus-crack extension data for center plane cross-sections of four specimens: (a) specimen #81 (CT, $B = 1/2$ -inch, $a/W = 0.75$), (b) specimen #C9 (CT, $B = 0.85$ -inch, $a/W = 0.5$), (c) specimen #E2 (CT, $B = 1/2$ -inch, $a/W = 0.5$), and (d) specimen #D6 (CCT, $B = 1/2$ -inch, $a/W = 0.5$). Note: the normalized depth is $2z/B = 0$ at surface and $2z/B = 1$ at center.

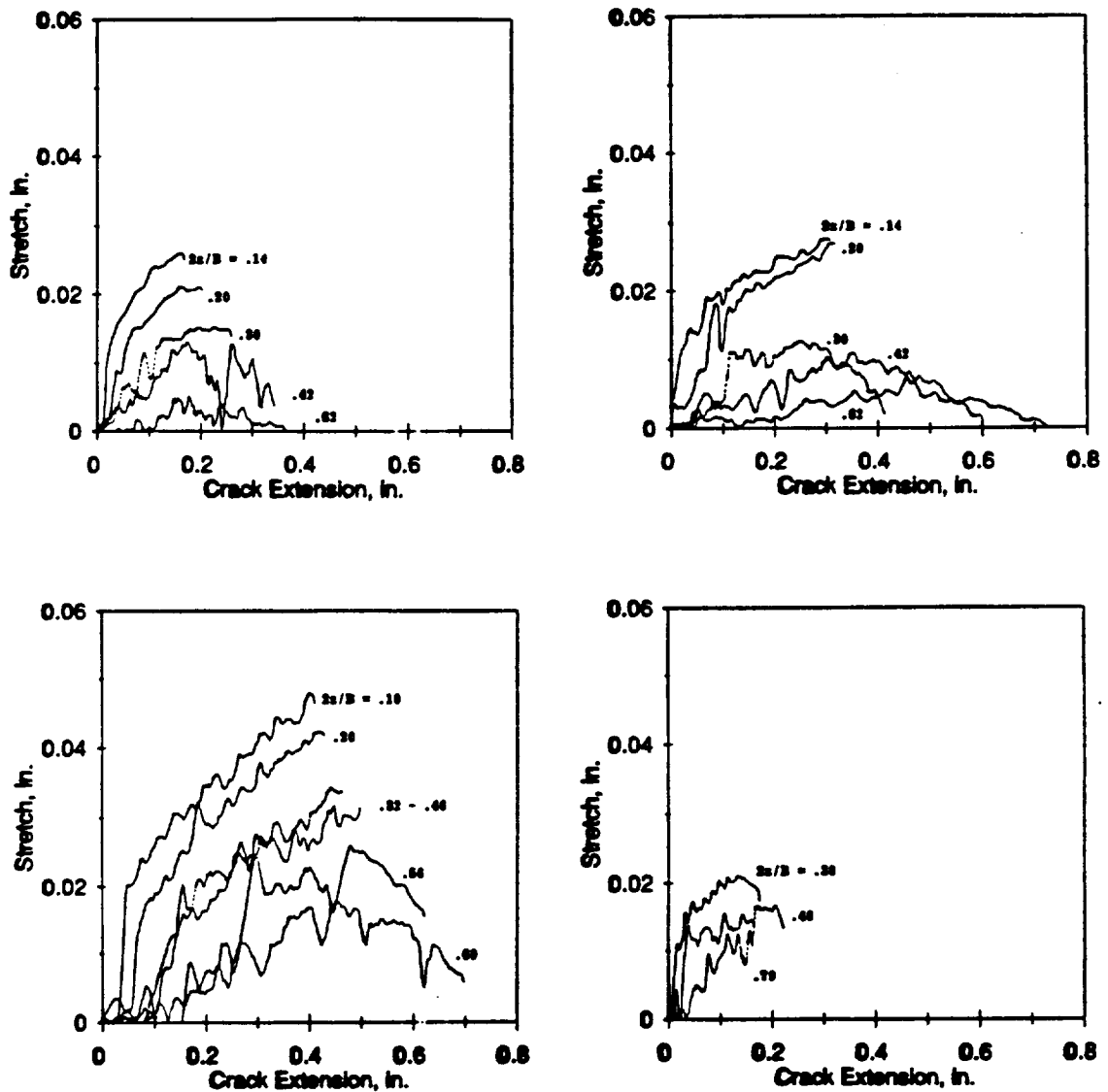


Figure 2.10: Stretch-versus-crack extension data for cross-sections from surface to center plane of four specimens: (a) specimen #81 (CT, $B = 1/2$ -inch, $a/W = 0.75$), (b) specimen #C9 (CT, $B = 0.85$ -inch, $a/W = 0.5$), (c) specimen #E2 (CT, $B = 1/2$ -inch, $a/W = 0.5$), and (d) specimen #D6 (CCT, $B = 1/2$ -inch, $a/W = 0.5$). Note: the normalized depth is $2z/B = 0$ at surface and $2z/B \approx 1$ at center.

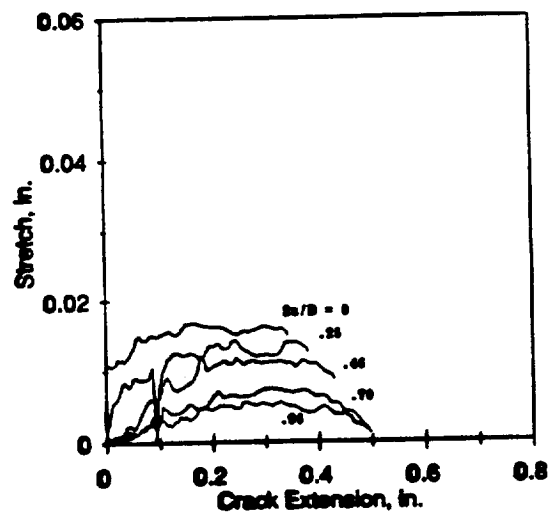
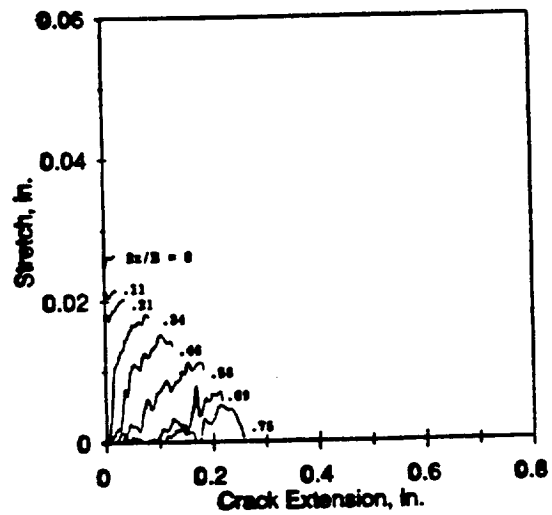


Figure 2.11: Stretch-versus-crack extension data for cross-sections from surface to center plane of two specimens: (a) specimen #84 (CT, $B = 1/2$ -inch, $a/W = 0.5$), and (b) specimen #51 (CT, $B = 1/4$ -inch, $a/W = 0.5$). Note: the normalized depth is $2z/B = 0$ at surface and $2z/B \approx 1$ at center.

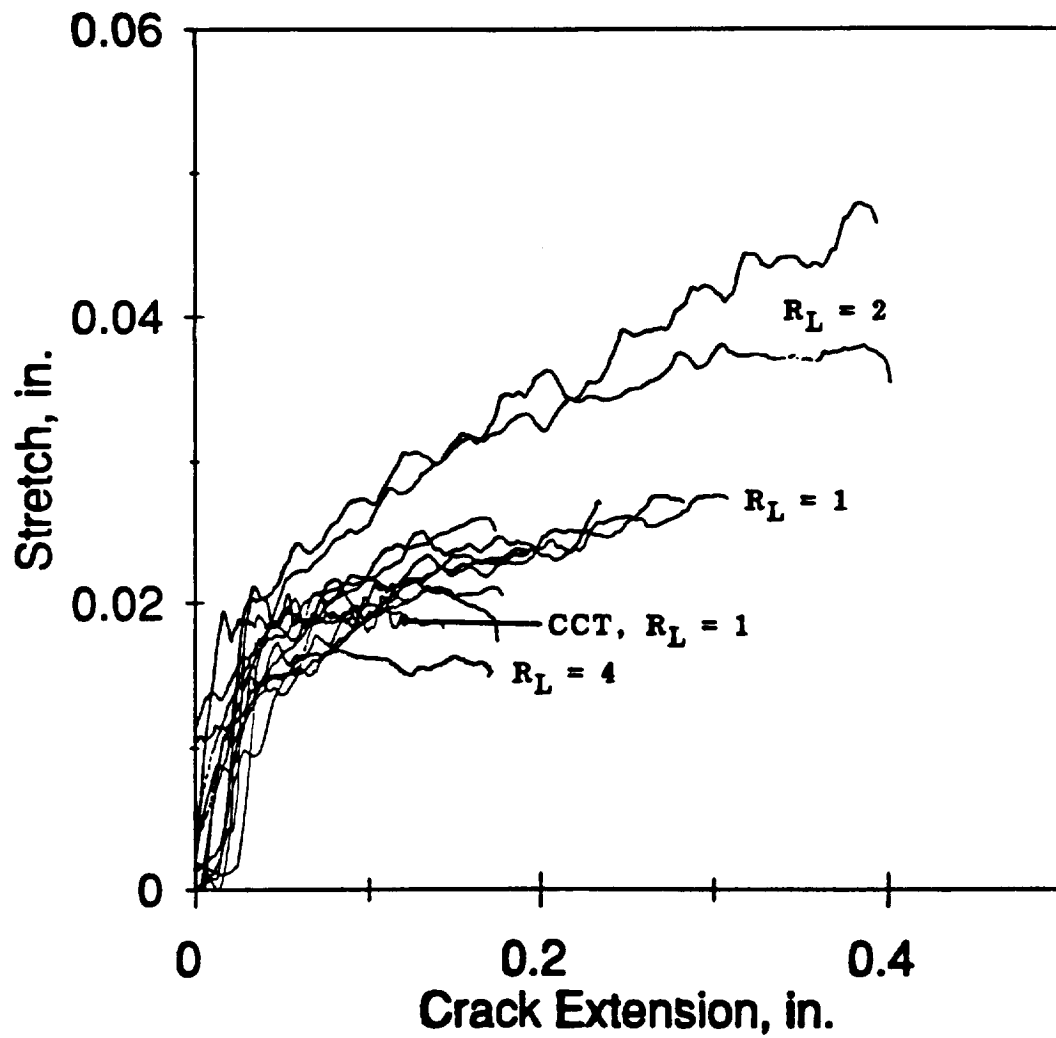
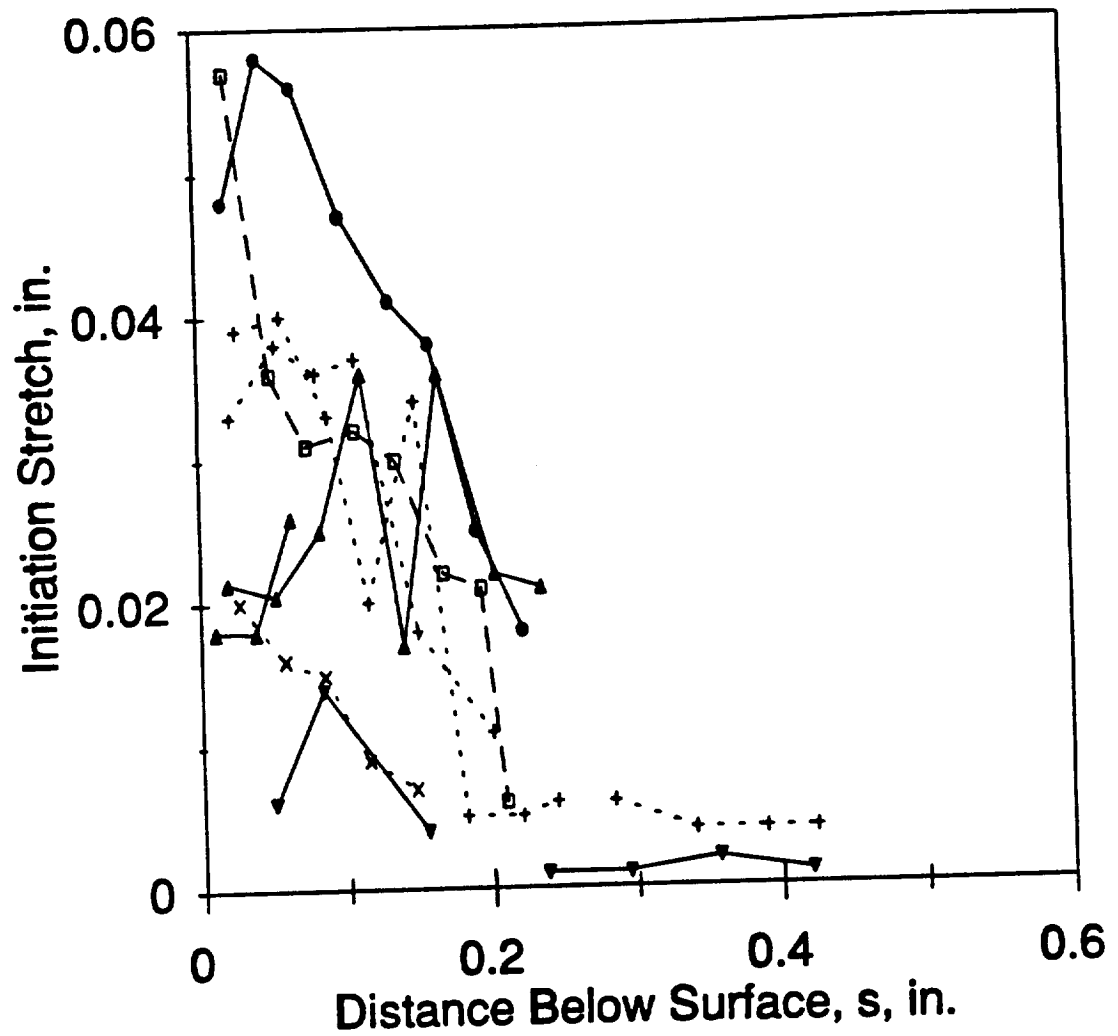
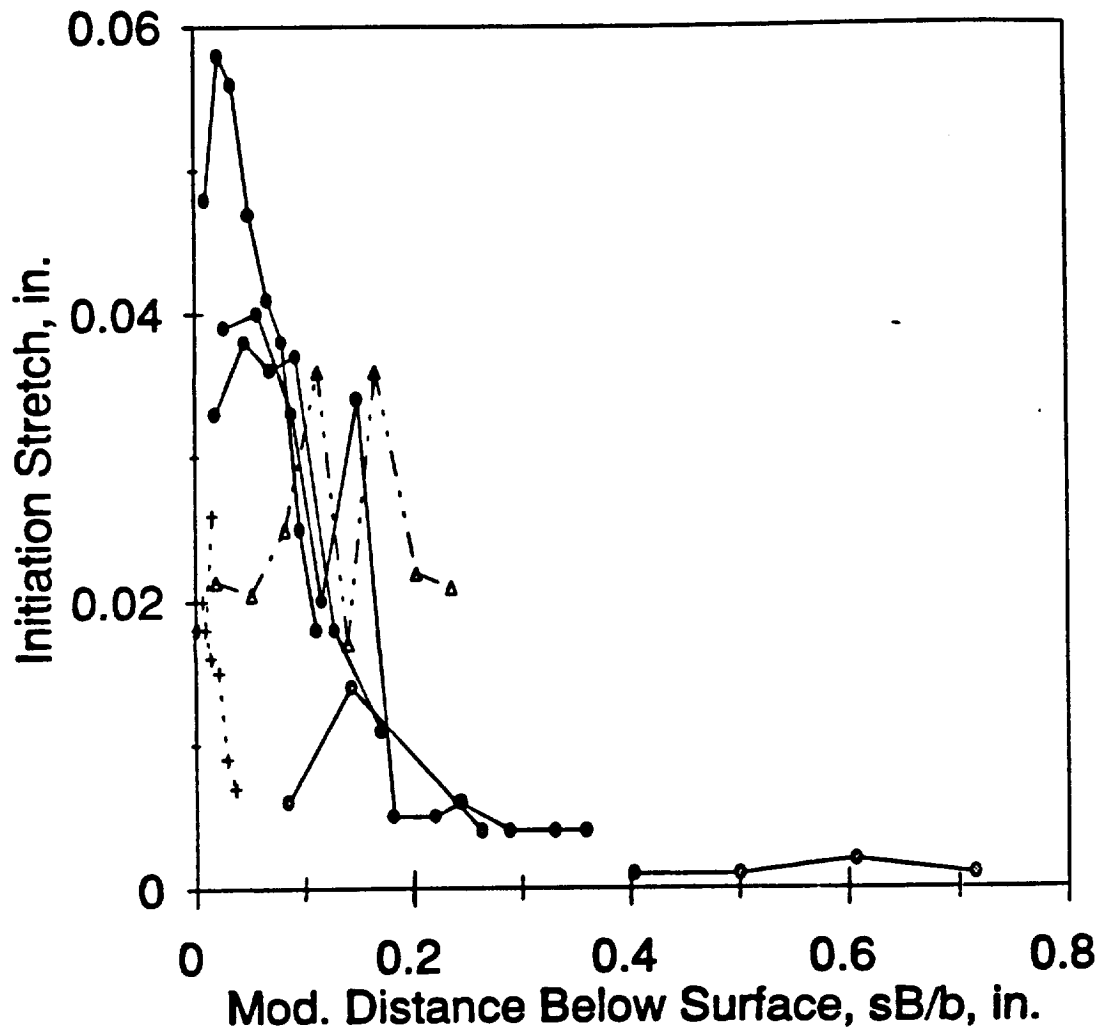


Figure 2.12: Comparison of stretch-versus-crack extension data for near surface cross-sections of various specimens: $R_L = 1, 2, 4$, and CCT with $R_L = 1$.



+ CT, $b/B=1$ □ CT, $b/B=2$ → CT, $b/B=2$
 × CT, $b/B=4$ → CCT, $b/B=1/2$ → CCT, $b/B=1$
 → CCT, $b/B=4$

Figure 2.13: Comparison of initiation stretch as a function s , the depth below the original specimen surface for a variety of specimens. Note: at surface, $s = 0$, and at center, $s = B/2$.



$\cdot +$ $b/B=4$ \rightarrow CCT, $b/B=1$ $\cdot +$ $b/B=4$

Figure 2.14: Comparison of initiation stretch as a function sB/b , the modified depth below the original specimen surface for a variety of specimens.

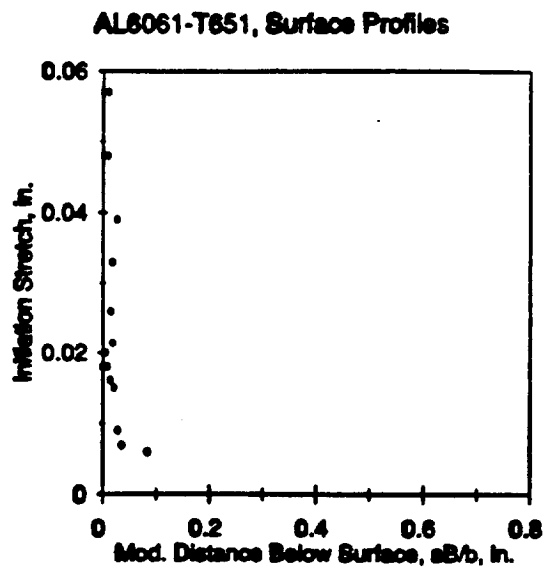
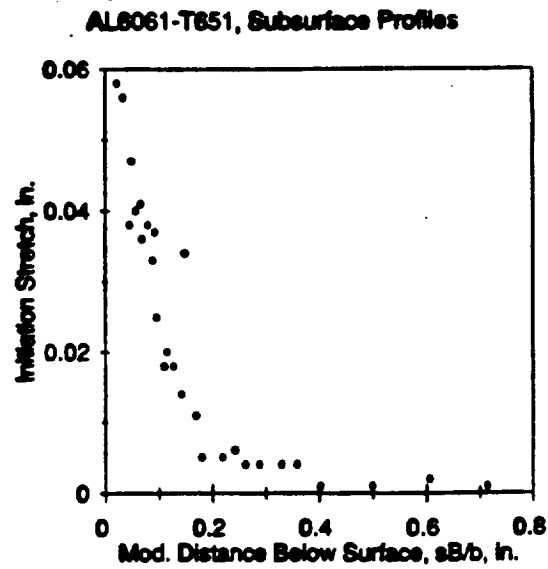


Figure 2.15: Comparison of initiation stretch as a function sB/b , the modified depth below the original specimen surface for a variety of specimens: (a) subsurface data (excludes first surface point, CCT data and $R_L = 4$ data), and (b) "surface data".

CHAPTER III

RESISTANCE CURVE ANALYSIS

by D. Lambert and H. Ernst

3.1 J and J_M Resistance Curve Analysis

In the literature, variations in the resistance curves of a given material have been reported for differently sized and shaped ligaments. This is due to the variations of constraint that occur for each configuration. To demonstrate the effects of constraint and for the purposes of this investigation, a test matrix was established that provided a wide variety of specimen configurations. The ranges of the configuration defining variables investigated appear in brief in Table 3.1.

The different configurations tested produced different groups of resistance curves for both materials investigated, and the purpose of this section is to present these qualified results. A close look at the valid portion of each of the resistance curves would show two features: (1) the qualified J-modified resistance curve extends much further in most cases than that of the J-integral resistance

curve, and (2) the J-integral and J-modified agree well up to the limit of J. It should also be noted that J-modified appears to be a smooth extension of the valid portion of the J-integral curve in each case.

3.1.1 JR and J_MR Curves for Compact Tension Specimens

Figure 3.1 suggested that certain specimens should be compared, and the basis for comparison of the aluminum results was using $R_L \equiv b_0/B$, while B was found to be appropriate for the IN718-STAl. The next set of figures (figures 3.2 and 3.3) correlates the valid J and the qualified J_M resistance curve data for the aluminum. The correlation has improved dramatically for both the J and the J_M curves.

Focusing on the J_M results at this point (figure 3.3), the curves chosen for comparison are very similar. Notice that the $R_L = 1/2$ and the side-grooved configurations are shown in figure 3.3a, while those for $R_L = 1$ appear in figure 3.3b, and those for $R_L = 2$ and 4 appear in figure 3.3c. In figure 3.3c, a slight variation exists between curves for $R_L = 2$ and $R_L = 4$. The curve variation could be due to configuration (R_L ratio) differences. This will be discussed, below. Figure 3.4 has been included to show the improved correlations and the presence of different behaviors of the J_M curves after qualifying the data. Three distinct curves of different slopes clearly are present in this graph. One of the side-grooved CT specimens shows data

more reminiscent of the $R_L = 1$ curves (specimen #E3, aluminum, CT, $W = 2$ -inches, $B = 1/2$ -inch, 20% side-grooved, $a/W = 0.5$): the side-groove was not directly on the precrack tip and the crack grew into the side-groove instead of starting there. The resulting crack front had considerable curvature, and a substantially higher resistance curve. Normally the side-grooved configuration produces a straight crack front, and this data is not thought to clearly fit into any particular category being investigated and will be ignored.

Next, the "valid" J_M data for the nickel alloy is presented in figures 3.5. A graph for the nickel alloy of thickness $B = 0.80$ -inches was excluded at this point, because only one specimen was represented, and no comparison was available. The data segregated onto each figure compares well. Figure 3.6 compares all of the qualified J -modified data for the nickel alloy including the specimen omitted earlier (specimen #A5, nickel, CT, $W = 2$ -inches, $B = 0.80$ -inches, $a/W = 0.5$), and after the qualifying step, four distinct curves are apparent. The imposing of the J_{MR} curve inflection point limitation as the final point of consideration of the data has provided good correlation with the qualified data.

The subsection that follows is devoted to a discussion of the results for the other two configurations used to analyze the fracture resistance of the AL6061-T651, namely center-crack tension and single-edge notch tension

specimens. This is followed by a section discussing the nickel CCT fracture behavior, and then a general discussion of all of the results.

3.1.2 Aluminum CCT and SENT Fracture Resistance Curves

The AL6061-T651 center-crack tension (CCT) specimen data were shifted in the same manner as the CT data, validity limits were imposed, and the results appear in figure 3.7. The early part of the CCT specimen J_{MR} curves appear to follow the apparent blunting line to a much higher value of J_M than was observed with the CT specimens. It must be noted that the center-cracked tension specimen with side-grooves (specimen #C0, aluminum, CCT, $2W = 2$ -inches, $B = 0.85$ -inches, 20% side-grooved, $a/W = 0.6$) underwent unstable fracture, and the data was developed by assuming that the crack curvature correction factor remained constant throughout the test. The resulting resistance curve fits the trend of the other data in figure 3.7, and this is considered to be a reasonable estimate, since the side-grooved configuration is thought to produce a consistently straight crack front. The thinnest specimen (specimen #55, aluminum, CCT, $2W = 2$ -inches, $B = 1/8$ -inch, shown as filled squares in figure 3.7) follows that of the thickest and the side-grooved specimens. This is not the behavior expected, but the data is thought to be bonafide.

The aluminum single-edge notch tension (SENT) specimen test results are shown in figures 3.8. The first graph,

figure 3.8a shows the SENT data separately, while the second, figure 3.8b shows a comparison of the SENT data superimposed on that of the CT specimen data. The SENT results are the filled symbols in figure 3.8b and are very similar to those of the aluminum CT specimens. The only difference apparent is that the SENT specimen with ligament proportion $R_L = 1$ follows the blunting line to a higher value of J than the CT specimen of the same R_L ratio. A closer scrutiny comparing the behavior of the aluminum for all three specimen types will be presented below.

Figure 3.9 shows the data for all of the aluminum specimens on one graph. The blunting line has been shown for reference. In this figure, the CT and the SENT specimens of equal R_L value would not be discernable from each other within a small range of variation of the graphs, and the CCT specimens do not deviate from the blunting line until much higher values of J_M .

3.1.3: Nickel CCT Fracture Resistance Curves

The IN718-STAl center-crack tension specimen data are shown in figure 3.10. The behaviors of both specimens are very similar in the upper end of the $J_M R$ curves. The early behavior of the nonside-grooved specimen (specimen #24, nickel, CCT, $2W = 2$ -inches, $B = 1/4$ -inch, $a/W = 0.5$) has been attributed to the imprecision with which the crack lengths were measured. Figure 3.11 compares the various compact tension specimen results with those of the center-

crack tension specimens. Also shown in this figure is the ASTM blunting line for this material. As was seen with the results from the aluminum specimens, the nickel CCT specimens follow the blunting line to much higher J levels. In this case, the data does not appear to deviate from the blunting line for the duration of both tests. A more in-depth discussion of the J_M resistance curve results follows.

3.1.4: Discussion of J_M Resistance Curve Results

Several characteristics that are very prominent in the adjusted curves should be discussed. The first comments are general, relating to both of the materials and focusing especially on the level of confidence in the data, on the success of J or J_M in correlating the data, and on the behavior of the specimens. These comments are followed by characterizations of the fracture behavior for the two materials and a discussion of the differences in the perceived behavior between the two materials.

The test data was rough, however this is not expected to invalidate the results or to reduce the impact of the conclusions drawn, herein. This roughness is thought to arise primarily due to imprecision associated with the determination of the intermediate crack lengths early in the test from measured unloading compliance values. The data still show definite trends, and all of the data is consistent with these trends with few exceptions. These exceptions will be mentioned at the appropriate time.

From the CT data, J_M seemed to produce results that were identical to the J-integral up to the established ASTM E1152-87 [3.1] limits of validity of J. A close look at the various JR- and J_MR -curves would suggest that the point of deviation of the JR and J_MR curves is very close to the same point indicated by the ASTM limit. One other possibility for the marker of the divergence point of J and J_M was the maximum load. This occurred consistently at a crack extension of five-percent of the initial ligament length. The difference in J and J_M grows to about three-percent of J at the ASTM limit (i.e., $\Delta a/b_0 = 0.1$). By limiting J_M data to include only data prior to the upwards inflection point visible in some J_MR curves, the correlation of the data was improved throughout the data set with the only apparent variations being due to experimental error, and the J_MR curve was a smooth extension of the JR curve beyond the limit of the J-integral. The physical phenomenon that becomes significant at the inflection point of J_M is believed to be the onset of large-scale plasticity, i.e., the saturation of plasticity into the back face of the specimen [3.2]. This subject was discussed earlier in this chapter.

Using J_M resistance curve data, the fracture performance of the AL6061-T651 specimens is summarized in figures 3.3, 3.7, 3.8a, and 3.9. For the CT specimens, no specific thickness or ligament length effect is obvious in the data. Instead, the fracture resistance was a function

of the ligament length-to-thickness ratio, b_0/B . Any secondary dependence of the fracture properties due to length or thickness of the ligament was overwhelmed by experimental error. Two sizes of the CT specimen configuration were used, and these were the 1/2T and the 1T configurations, associated with planar dimensions defined by $W = 1$ -inch and $W = 2$ -inches, respectively. No difference in the results was found between these two configurations. The CCT and SENT specimens used the same initial ligament length, thus the ligament length, thickness, and proportion effects are not separable in the results. If expressed as a function of the ligament proportion, the trend of all data was identical to that of the CT specimens, i.e., the fracture behavior of the aluminum CT, CCT, and SENT specimens appear to be controlled by the ligament length-to-thickness ($R_L \equiv b_0/B$) ratio. The observed behavior of the $B = 1/8$ inch CCT specimen (#55, aluminum, CCT, $2W = 2$ -inches, $B = 1/8$ -inches, $a/W = .5$) will be noted here as the one exception.

Looking at figure 3.3a, aluminum CT specimens with $R_L = 1/2$ yields behavior identical to that of the plane strain CT specimens (side-grooved configuration). Next, looking at figure 3.3c, CT specimens with $R_L = 2$ and $R_L = 4$ appear to produce equivalent results to each other. Figure 3.4 shows all of the aluminum CT specimen results on one graph. The curves become more steeply inclined as R_L increases. However, the behavior of the J_M R-curves seems to start from

a "saturated" value of plane strain that is present for the side-grooved and the $R_L = 1/2$ specimens, and then the curves appear to "saturate" again to a value that is taken to be plane stress when $R_L \geq 2$. Thus, an active region of changing constraint for the aluminum alloy appears to be plane strain = $1/2 \leq R_L \leq 2$ = plane stress. Within these limits, the average constraint is between plane strain and plane stress.

The fracture performance of the IN718-STAl CT specimens is summarized in figures 3.5 and 3.6 and figures 3.10 and 3.11. The fracture behavior of the nickel alloy is not defined by the ligament proportion as is the aluminum, but is characterized by the ligament thickness, B. This is true for the CT specimens tested, but the nickel CCT specimens were limited to one thickness ($B = 1/4$ inch and $B = 1/4$ inch, with side-grooves), and no deviation from blunting line behavior was obvious in either case (figure 3.11).

In figure 3.5a, the J_{MR} curve for the nickel CT specimen with the longest ligament (specimen #14, nickel, CT, $W = 2$ -inches, $B = 1/4$ -inch, $a/W = 0.5$, i.e., $b_0 = 1$) appears to be slightly higher than those for specimens with shorter ligaments, but this is thought to be associated with experimental error and can be easily influenced by the shifting discussed early in this section. Figure 3.6 combines all of the nickel CT data to compare the results.

The nickel J_{MR} curves are found to incline more steeply as the specimens become progressively thinner. Figure 3.12

has been included to compare the results of the plane strain condition (side-grooved configuration) to those of the thickest specimen (specimen #A5, nickel, CT, $W = 2$ -inches, $B = 0.8$ inch, $a/W = 0.5$). The axes are greatly expanded in this case, and the behavior of the $B = 0.8$ inch specimen appears to continue rising while that of the side-grooved specimens appears to be constant. A thickness of $B = 0.80$ -inches should not be considered to be exhibiting plane strain fracture.

The results of all of the CCT and SENT data are summarized in figures 3.7 - 3.9 (aluminum), and figures 3.10 and 3.11 (nickel). The data for the CCT specimens was somewhat truncated, because unstable cleavage seemed to occur with only a small amount of crack growth. It should be noted that in all cases, the thickness was varied and the ligament length was kept the same at $b_0 = 1/2$ inch.

The aluminum CCT specimen data appears in figure 3.7. With the exception of the thinnest specimen (filled square symbols, specimen #55, aluminum, CCT, $2W = 2$ -inches, $B = 1/8$ -inches, $a/W = 0.5$), the J_{MR} curves of the remaining specimens show different slopes, behavior congruent to the CT behavior: the specimen with side-grooves and the one with the lowest value of ligament proportion ($R_L = 1/2$) produce the lowest curves, while for increasingly higher values of R_L , the JR and J_{MR} curves are increasingly higher. The behavior of the thinnest specimen (#55) was not as anticipated, however all of the other specimens provide

consistent behavior. It appears that the thickest specimen (specimen #B9, CCT, $2W = 2$ -inches, $B = 0.85$ -inches, $a/W = 0.5$) was sufficiently thick to produce plane strain behavior, however with the behavior of the thin specimen and with the sparsity of the data, conclusions cannot be stated as strongly as with the compact tension specimens. The aluminum CCT data does follow the same trend as that of the aluminum CT specimens, though, and the correlation of behavior with respect to R_L appears similar. One large difference between the CCT and CT results is that curves for the CCT specimens diverge from the blunting line at a much higher value of J_M than do the curves for the CT specimens (figure 3.8).

The SENT specimen configurations were quite similar to some of the CT specimens. The SENT specimen has a large distance between the loading points, and the specimen halves will not rotate as the test proceeds to large displacements and long crack lengths. The results of the SENT specimens are similar to those of the CT specimens with similar R_L -value, except that the SENT configuration continues to a higher J_M -value before diverging from the blunting line (figure 3.7b).

The nickel CCT specimens follow the blunting line to a much higher level of J_M than the CT specimens before showing any deviation from the blunting line. In fact, the two nickel CCT specimens tested did not show any deviation from blunting line behavior for the limits imposed on the test.

The aluminum and the nickel show dramatic differences in fracture behavior. The aluminum specimens showed fracture behavior controlled by $R_L = b_0/B$, and it appears that at $R_L = 1/2$, the behavior is equivalent to that of plane strain (side-grooved) specimens. If R_L is increased from $1/2$, the JR and J_M R curves become higher, up to a point. The curves of $R_L = 2$ are roughly equivalent to that of $R_L = 4$. This suggests that at $R_L = 2$, the ligament is subjected to plane stress fracture or the surface effect has saturated the ligament, and that fracture behavior will no longer change as R_L continues to increase. The nickel specimens were effected by thickness B, alone.

The behavior of the nickel is quite different: over the range of compact tension specimen configurations tested, the fracture behavior of IN718-STAl changes with thickness, only. Figure 3.13 suggests that the resistance curves for the IN718-STAl compact tension specimens of ligament proportion $R_L = 1$ differ greatly.

3.2 Power-Law Fit of R-Curve Data and J_{IC} Estimates

For each specimen, the qualified JR and J_M R data showed good agreement, although the limiting of the JR-curve to a crack extension of ten-percent of the initial remaining ligament length allowed a slight divergence between J and J_M . The resulting R-curves showed certain common behaviors, and the aluminum and the nickel alloys exhibited different

characteristics: specifically, the aluminum data were identical for equal ligament initial length-to-thickness ratio, $R_L \equiv b_0/B$, while the nickel data aligned for like ligament thickness, B . The R-curves for the aluminum CT specimens exhibited an increasing slope as R_L increased, while the R-curves for the nickel inclined more steeply as the ligament thickness decreased.

Little redundancy was included in the matrix of CCT test specimens and all of these specimens had the same initial remaining ligament length, thus thickness and R_L -proportion effects could not be separated. The aluminum CCT specimen data did produce increasing slope of the R-curves for increasing R_L (or alternately for decreasing thickness, B), this is the same characteristic R-curve slope trend as the aluminum CT specimens. The nickel CCT specimens seemed to follow the blunting line, although the results of a regression analysis of the data has been included.

The correlated data were fitted to a power law form:

$$J_M = J_0 \cdot (\Delta a)^m \quad (3.1)$$

In equation 3.1, Δa is the crack extension and J_0 and m are fitted constants from a linear regression analysis of the relationship of the logarithms of J_M and Δa . The fit was performed only for J_M because the common bases for comparison (R_L for aluminum and B for nickel) arose in the J_M analysis, not in the J-integral analysis. The fitting

procedure used all of the qualified and correlated data in each case. The results of the regression analysis appear in tables 3.2 and 3.3, below.

The data in table 3.2 generally show a consistent trend for both J_0 and for m within the specimen types, except for the CCT specimen with $R_L = 2$. The data for this specimen was observed to follow the blunting line, and the value of $m = 1.01$ appears to corroborate this. Generally, the values for the exponent m for the CT or for the CCT specimens should be considered to be relatively equal, except that the side-grooved configurations (marked "SG") have exponents that are noticeably lower than the nonside-grooved specimens. The crack extension will be large for a small increment of J_M relative to the other configurations once the loading increases beyond the initiation value of J_M . The exponents, m , for the CCT specimens appear to be slightly higher than those of the compact tension specimens, but this may not be an appropriate conclusion: the difference may be a result of the fewer numbers of data points for the CCT, the relatively limited crack growth in the CCT specimen configurations, or some problem in providing an appropriate estimate of the average crack length.

The regression analysis results for the nickel are self-consistent and follow the same trend as those described for the aluminum. The values of J_0 are much larger in this case, reflecting the higher toughness of the nickel. The

exponent m also appears to decrease more over the range of configurations than the aluminum. For $B = 1/4$ -inch nickel specimens, the CCT data and the CT data have approximately the same exponent, but the different coefficients mean that the CCT requires four times the J_M input of the CT to produce identical crack extension. This was not as obvious with the aluminum results.

The regression analysis results for the compact tension specimen configurations have been presented graphically in figures 3.14, and the fits appear to be good in all cases.

The aluminum compact tension specimen data were investigated further to determine if any thickness effect was exhibited. No trend could be seen in the various data, and thus it is concluded that no observable thickness effect is present. The IN718-STAl data was treated similarly, but it was apparent that B alone defines the nickel CT behavior.

In summary, the data in tables 3.2 and 3.3 could be used for design purposes by matching similar ligament configurations. The fit functions were used to determine the value of J_{IC} for each configuration, and the results are summarized, below. The J_{IC} estimate is the intersection of the power-law fit functions from the tables, above, with a line of slope equal to twice the flow stress and offset by .008-inches (0.2-millimeters):

$$J_k = J_o \cdot (\Delta a)^m = 2 \cdot \sigma_o \cdot (\Delta a - .008) \quad (3.2)$$

This is the procedure recommended in ASTM E813-87 [3.3]. Mathematically, J_{IC} is derived from an iterative process, and the results appear in tables 3.4 and 3.5.

The values of J_{IC} varied through the complete range of ligament configurations of the aluminum compact tension specimens, although $R_L = 4$ and $R_L = 2$ results were virtually identical. This did not agree with the literature [3.4] where it had been suggested that J_{IC} is a constant. The regression analysis was generated from relatively extensive crack growth, but the results were thought to be bonafide and applicable to the determination of J_{IC} . Too much deviation occurs between the extremes to suggest that an averaging would be appropriate or that the value is a constant. The estimates in this case were derived from J_M , but the results were virtually the same using the individual specimen J-integral results. Applying the same procedures to the aluminum CCT specimen results provided different approximations, although J_{IC} for the $R_L = 1/2$ CCT and the side-grooved CCT configurations were the same.

A look at the J_{IC} results for the nickel alloy provided the same impression (table 3.5). The estimate of J_{IC} for the $B = 0.80$ -inch configuration and the side-grooved configuration are identical, but the thinner configurations have much higher estimates of J_{IC} .

The reason for the discrepancy between the data and the literature is unknown, but inspection of figures 3.14 suggests that the differences do exist. It seems reasonable

to assume that the extent of the adjustments from the crack lengths derived from the calibration functions and the unloading compliances to the average physical crack lengths may be involved, but the good agreement of the data adjusted in this fashion suggests that this would not be the cause of the variations of J_{IC} from configuration to configuration.

3.3 Conclusions and Recommendations

1. The qualified J_M R-curve data of AL6061-T651 compact tension specimens followed R_L , the ratio of the ligament length-to-ligament thickness. Shorter ligament lengths relative to the thickness are characterized by lower values of R_L , and these configurations provide results that are close to plane strain.
 - a) A constraint condition of plane strain was reached when R_L was reduced to $R_L \approx 1/2$. The plane strain condition corresponded to the lowest and flattest of the J_M R-curves and was approximated by compact tension specimen tests for a side-grooved configuration (10-percent per side).
 - b) The condition of plane stress corresponded to the highest and steepest of the J_M R-curves and this was reached by most of the aluminum CCT

specimens, which appeared to follow the blunting line to high values of J_M .

- c) For aluminum CT specimens, a stable response was reached when R_L was increased to $R_L \approx 2$. When R_L was increased beyond this, no further increase of the $J_M R$ -curve slope was apparent. The $J_M R$ -curve generated was lower than that of plane stress, and this was associated with the gradient of constraint from the surface to the center for CT specimens.
2. For the IN718-STAl, nickel alloy, the basis for comparison of the constraint, was the thickness.
- a) The fracture resistance associated with plane strain was estimated by testing side-grooved compact tension specimens. The constraint condition of this greatest thickness ($B = 0.85$ -inches) was not equal to plane strain, but was slightly higher, indicating a lower constraint than plane strain.
 - a) The CCT specimens followed the blunting line and are taken as the plane stress condition.
 - b) The CT specimens with the thinnest ligament section provided the steepest $J_M R$ -curve, but these did not follow the blunting line.
3. The $J_M R$ curve results have been provided in Chapter IV, and a regression analysis has been conducted with results presented in tables 3.2 and 3.3. The

power-law functional form produced good agreement with the J_{MR} -curve data.

4. The estimates for J_{IC} were not constant for the variety of configurations tested. J_{IC} was estimated using the ASTM procedure [3.1], and the results appear in tables 3.4 and 3.5.
5. The J_{MR} -curve data generated in standard fracture tests should be subjected to qualification using a validity limits criterion. The best technique was the inflection point of the J_{MR} -curve.
6. J_{MR} is recommended for the evaluation of fracture behavior over the J-integral because correlation is extended to a much higher degree of evolution of the fracture process.

3.4 References for Chapter 3

- [3.1] "Standard Test Method for Determining JR-Curves", ASTM Standard E-1152-87, 1989 Annual Book of ASTM Standards, Vol. 03.01 (1989), pp. 814-24.
- [3.2] Rice, J. R., Drugan, W. J., and Sham, T.-L., "Elastic-Plastic Analysis of Growing Cracks", Fracture Mechanics: 12th Conference, ASTM 700 (1980), pp. 189-221.
- [3.3] "Standard Test Method for J_{IC}, A Measure of Fracture Toughness", ASTM Standard E-813-87, 1988 Annual Book of ASTM Standards, Vol. 03.01 (1988), pp. 686-700.
- [3.4] Hellman, D., and Schwalbe, K. H., "Geometry and Size Effects on JR- and δR -Curves Under Plane Stress Conditions", ASTM STP 833 (1984), pp. 577-605.

3.5 Tables for Chapter 3

Table 3.1: Summary of Variables and Ranges, Task I

Materials Selected	AL6061-T651, aluminum alloy IN718-STA1, nickel-base super alloy
Ligament Thickness	$0.25 \leq B \leq .85$ inches
Ligament Length	$.25 \leq b_o \leq 1.0$ inches
Ligament Proportion	$.5 \leq b_o/B \leq 4$
Specimen Types	1/2T and 1T compact tension with $.5 \leq a_o/W \leq .75$, (bending with some tension), Center-crack tension, $2W = 2$, $a_o/W = .5$, (pure tension), Single-edge notch tension, $W = 2$, $a_o/W = .75$, (bending plus tension, intermediate to the other two)
Side-Grooving	Side-grooved or no

Table 3.2: Regression Analysis for AL6061-T651 Specimens

Configuration	J_o	m
CT, $R_L = 4$	2381	.574
CT, $R_L = 2$	2194	.565
CT, $R_L = 1$	1440	.505
CT, SG or $R_L = 1/2$	557	.376
CCT, $R_L = 4$	8189	.826
CCT, $R_L = 2$	47,544	1.01
CCT, $R_L = 1$	14,760	.671
CCT, $R_L = 1/2$	9379	.725
CCT, SG	3092	.467

Table 3.3: Regression Analysis for IN718-STA1 Specimens

Configuration	J_o	m
CT, $B = 1/4$ -inch	10,599	.562
CT, $B = 1/2$	4232	.457
CT, $B = 0.80$	2370	.395
CT, SG	1333	.272
CCT, SG and $B = 1/4$	46,299	.606

Table 3.4: Estimation of J_{IC} for AL6061-T651

Configuration	J_{IC}
CT, $R_T = 4$	168.0 psi-in
CT, $R_T = 2$	158.1
CT, $R_T = 1$	134.7
CT, SG and $R_T = 1/2$	94.6
CCT, $R_T = 4$	182.8
CCT, $R_T = 2$	---
CCT, $R_T = 1$	1039
CCT, $R_T = 1/2$	387.5
CCT, SG	383.6

Table 3.5: Estimation of J_{IC} for IN718-STAl

Configuration	J_{IC}
CT, B = 1/4-inch	709.1 psi-in
CT, B = 1/2	462.6
CT, B = 0.80	354.3
CT, SG	357.9
CCT, B = 1/4 and SG	---

3.7 Figures for Chapter 3

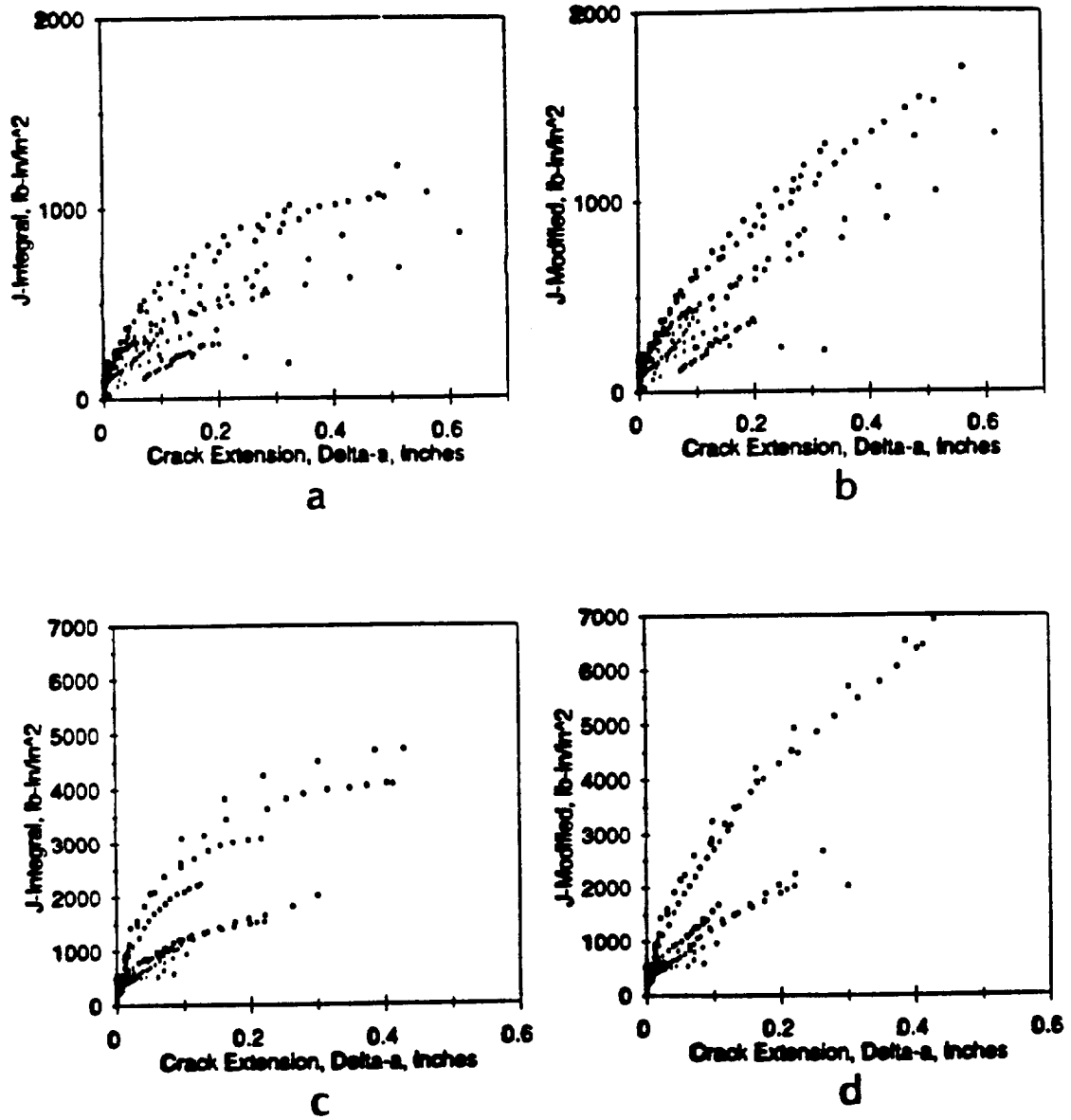


Figure 3.1: Collections of the JR and J_M R behavior of Task I AL6061-T651 and IN718-STA1 fracture specimens: (a) JR curve and (b) J_M R curve data, all aluminum CT specimens, (c) JR curve and (d) J_M R curve data, all nickel CT specimens.

Qualified JR Data for AL6061-T651 Compact Tension Specimens

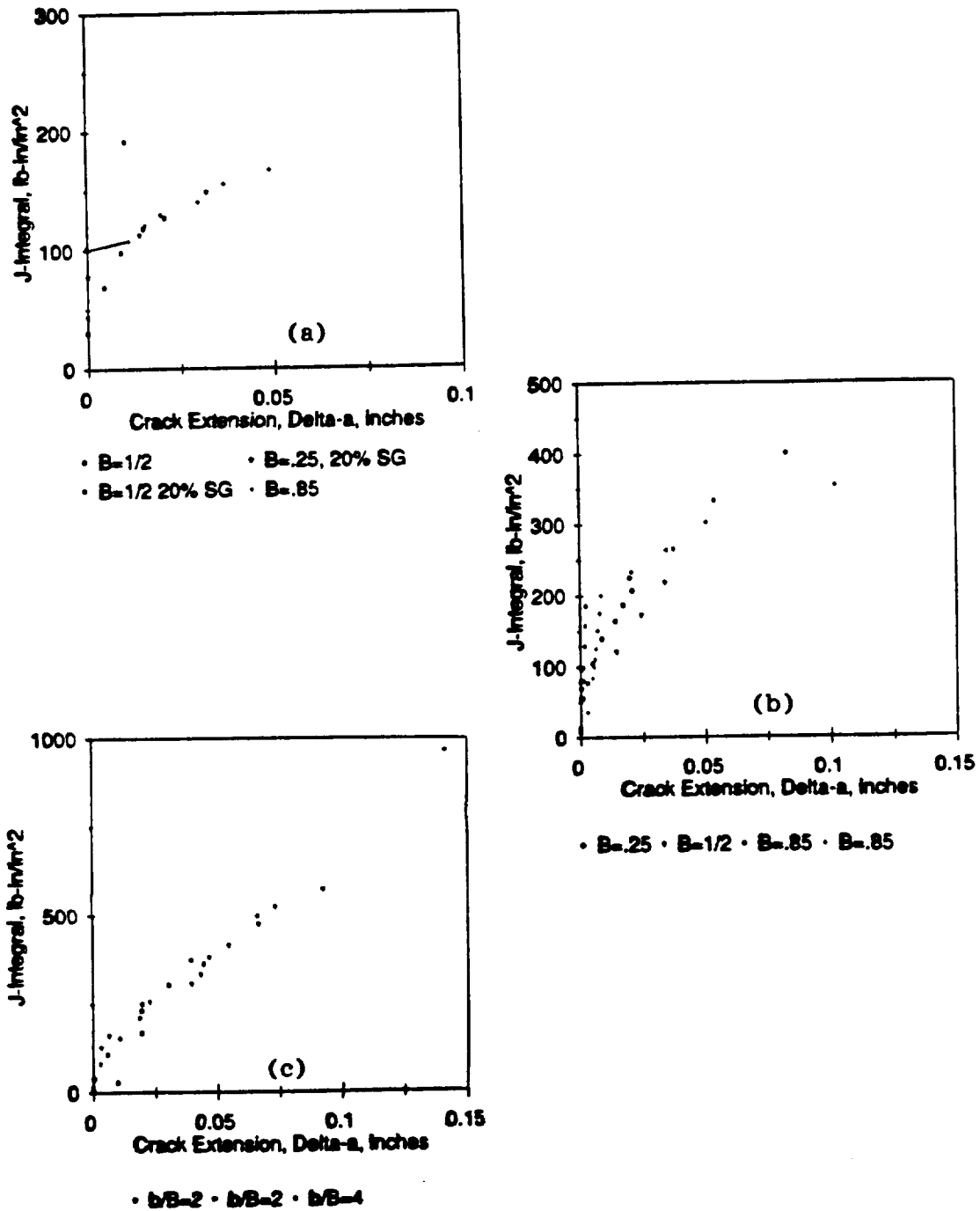


Figure 3.2: Collections qualified J resistance curves for AL6061-T651 compact tension specimens with similar ligament proportions: (a) $R_L = 1/2$ or side-grooved, (b) $R_L = 1$, and (c) $R_L = 2$ and $R_L = 4$.

Qualified J_M R Data for AL6061-T651 Compact Tension Specimens

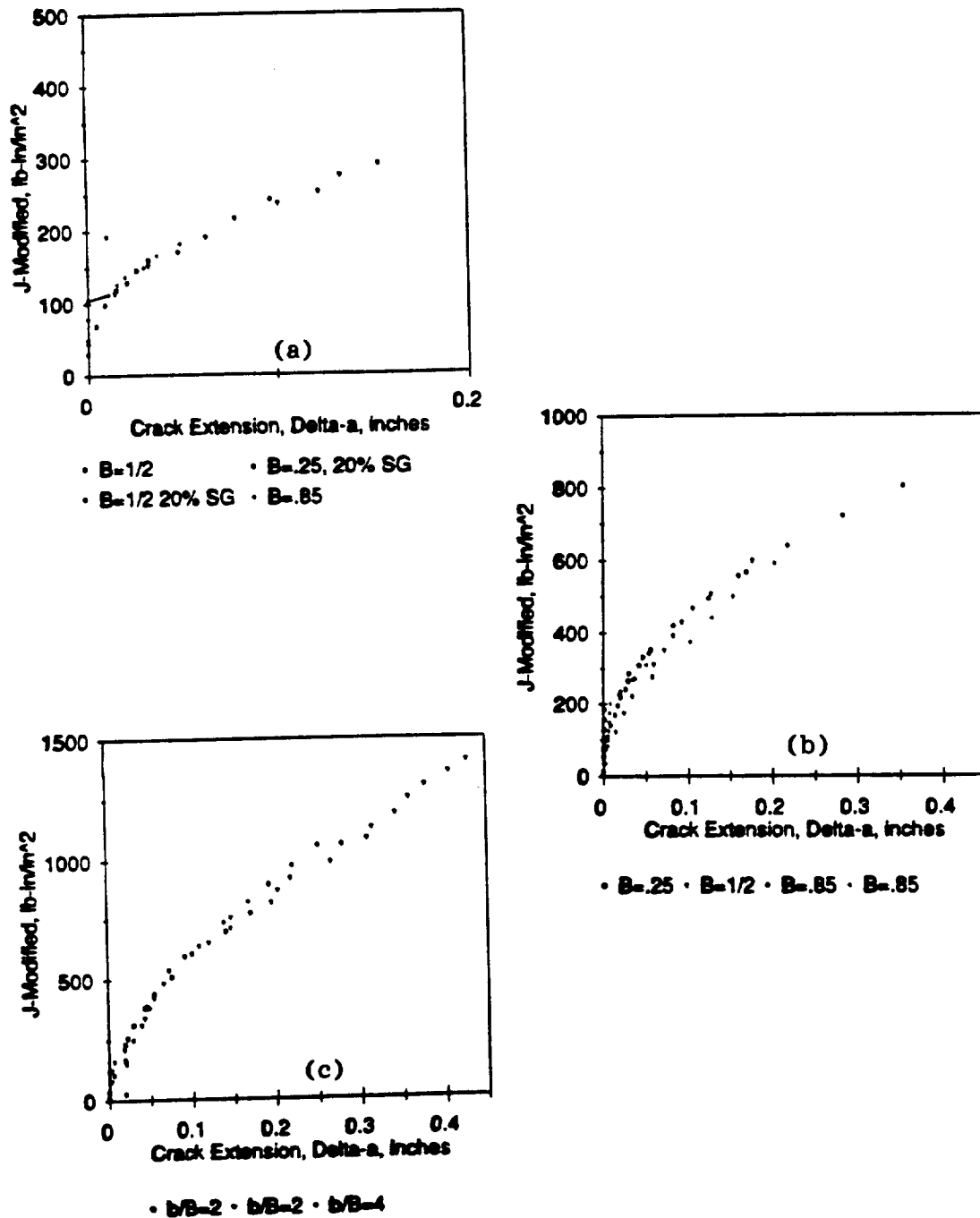


Figure 3.3: Collections of qualified J_M resistance curves for AL6061-T651 compact tension specimens with similar ligament proportions: (a) $R_L = 1/2$ or side-grooved, (b) $R_L = 1$, and (c) $R_L = 2$ and $R_L = 4$.

Qualified $J_M R$ Data for AL6061-T651 Compact Tension Specimens

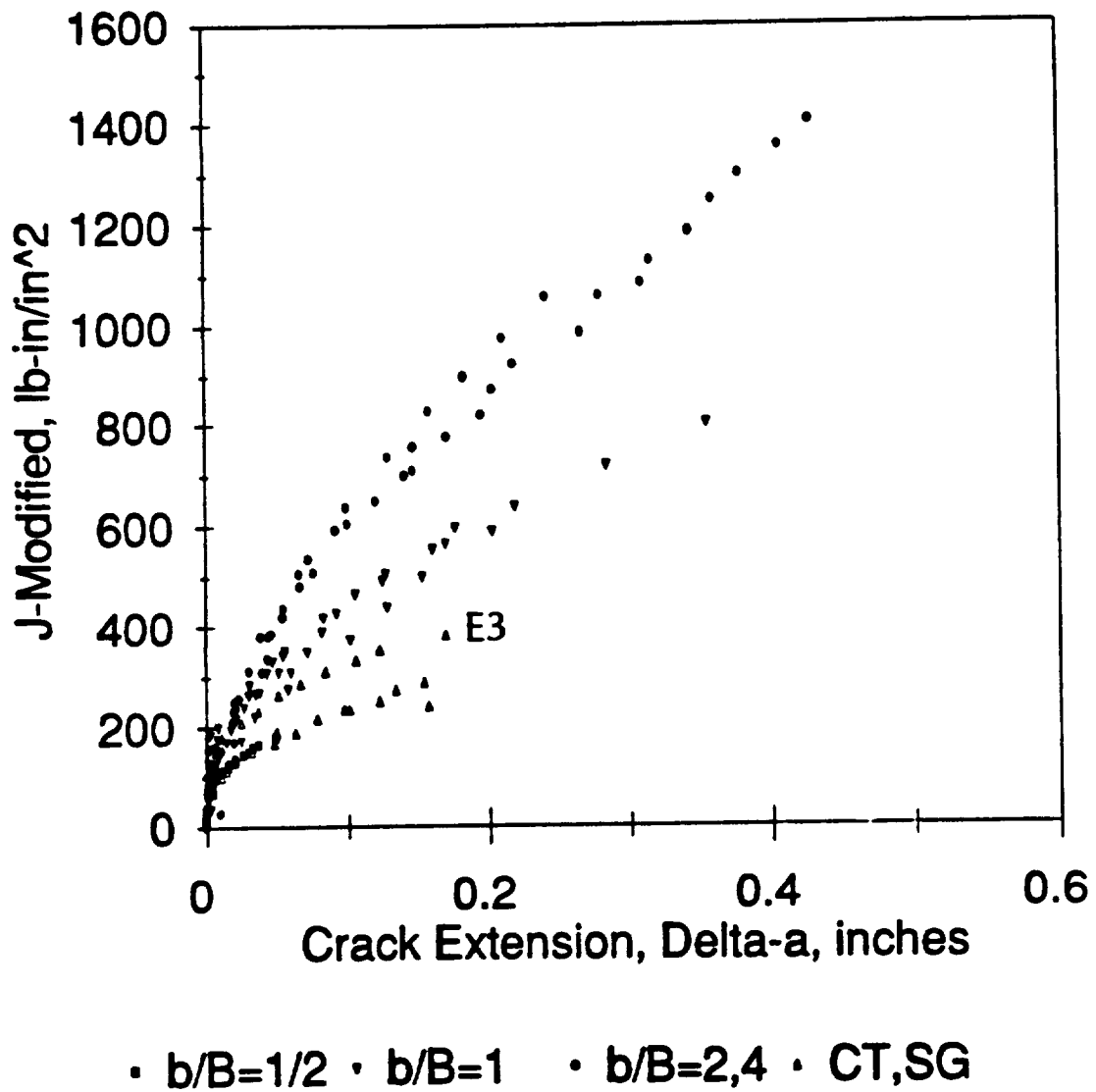


Figure 3.4: Collection of qualified $J_M R$ curves for AL6061-T651 compact tension specimens comparing different ligament proportions, R_L .

Qualified J_M R Data for IN718-STA1 Compact Tension Specimens

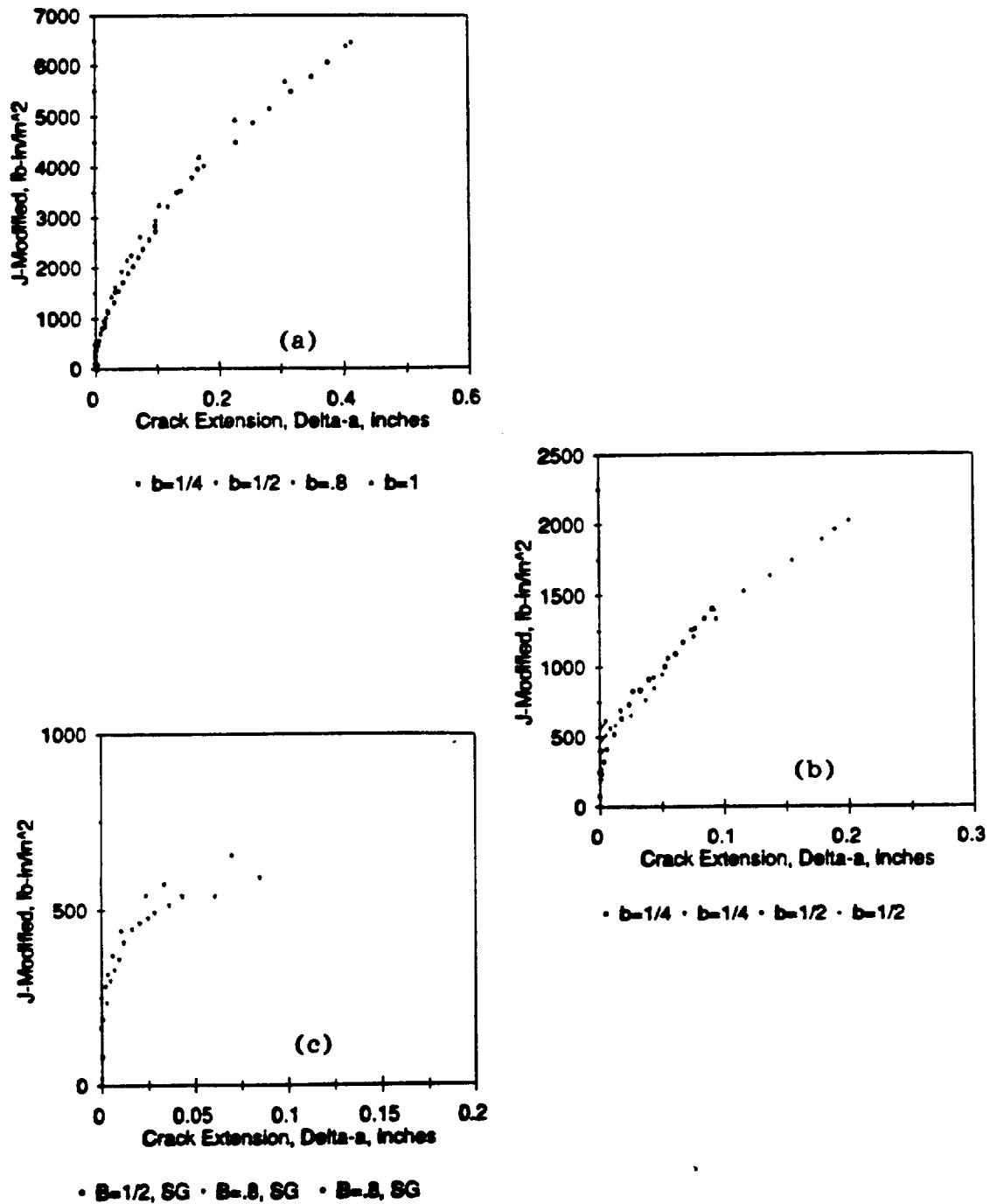


Figure 3.5: Collections of qualified J_M resistance curves for IN718-STA1 compact tension specimens with similar ligament thicknesses or side-grooved: (a) $B = 1/4$, (b) $B = 1/2$, and (c) side-grooved.

Qualified J_M R Data for IN718-STA1 Compact Tension Specimens

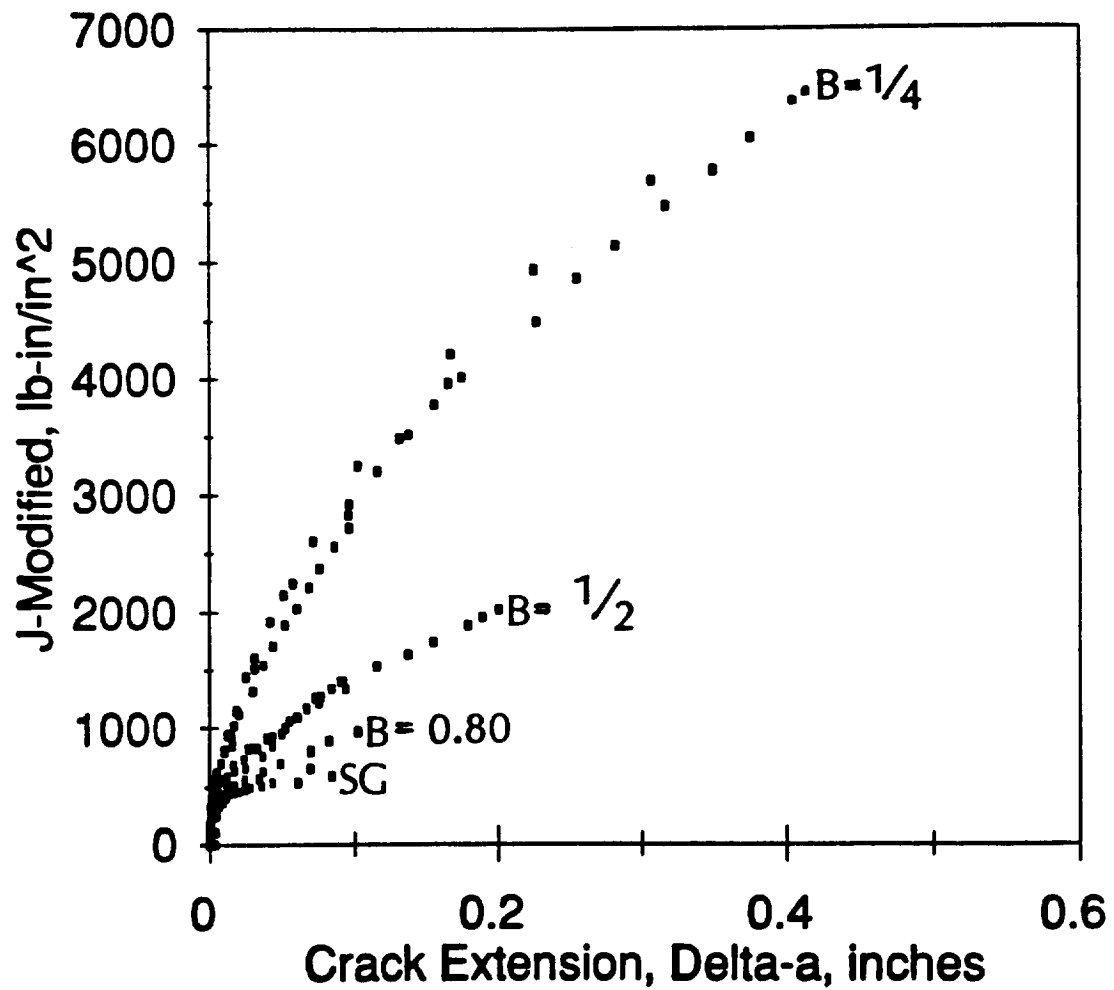


Figure 3.6: Collection of qualified J_M R curves for IN718-STA1 compact tension specimens comparing different ligament thicknesses, B.

Qualified $J_M R$ Data for AL6061-T651 Center-Cracked Tension Specimens

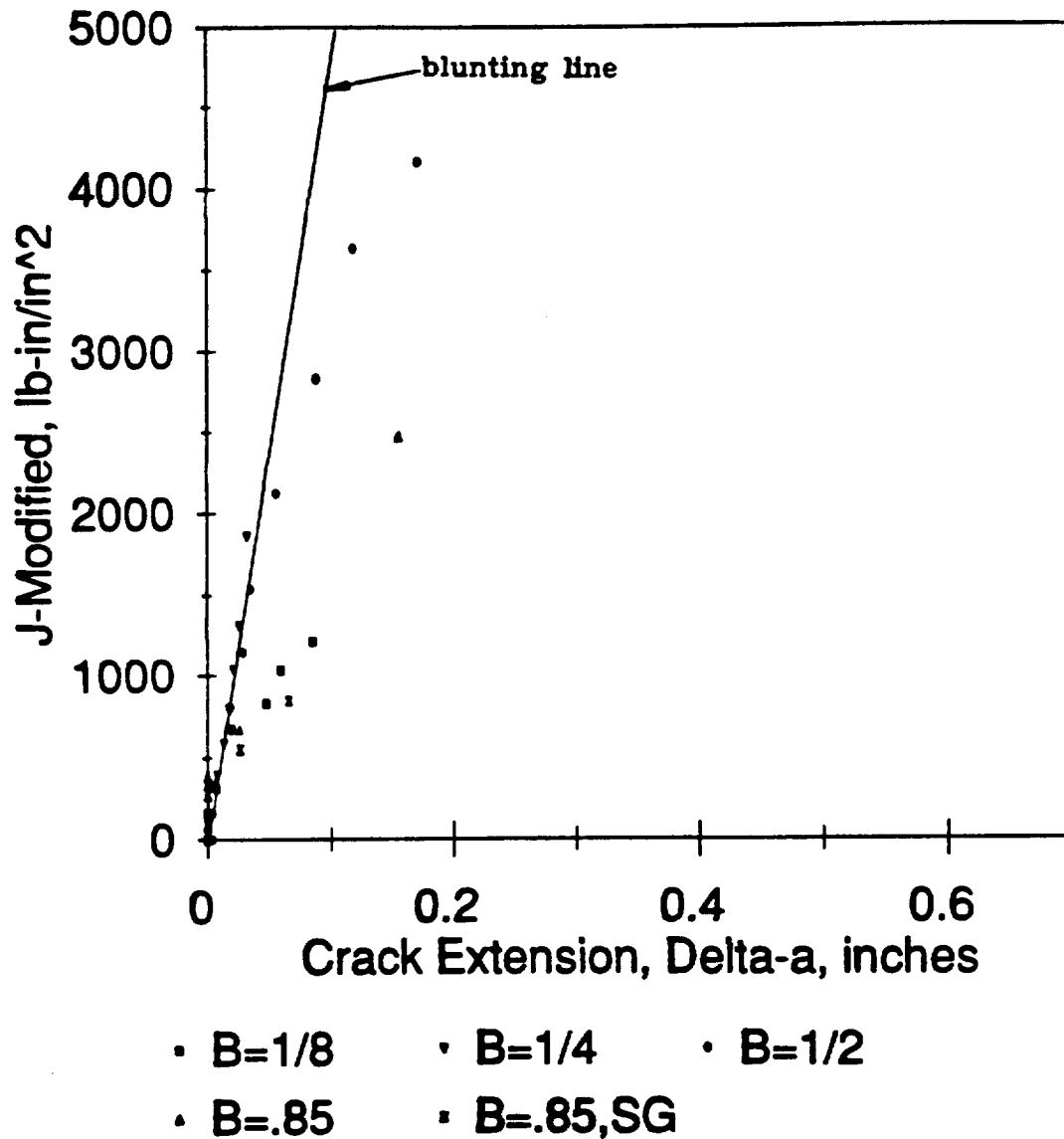


Figure 3.7: Qualified $J_M R$ curves for AL6061-T651 center-cracked tension specimens comparing different ligament thicknesses, B , (or equivalently ligament proportions, R_l) with constant ligament length, $b = 1/2$ - inch.

Qualified J_M R Data for AL6061-T651 Specimens

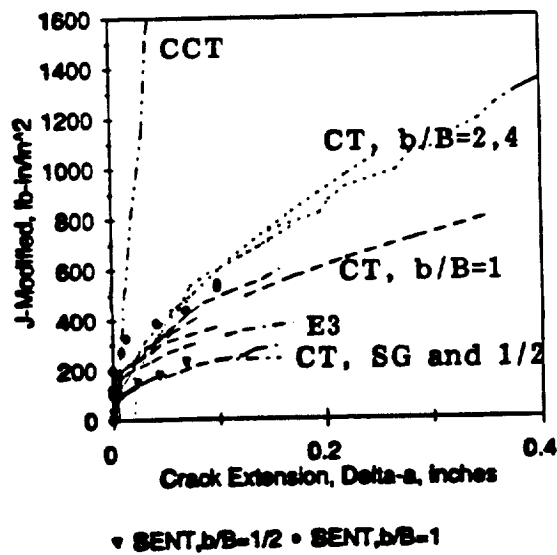
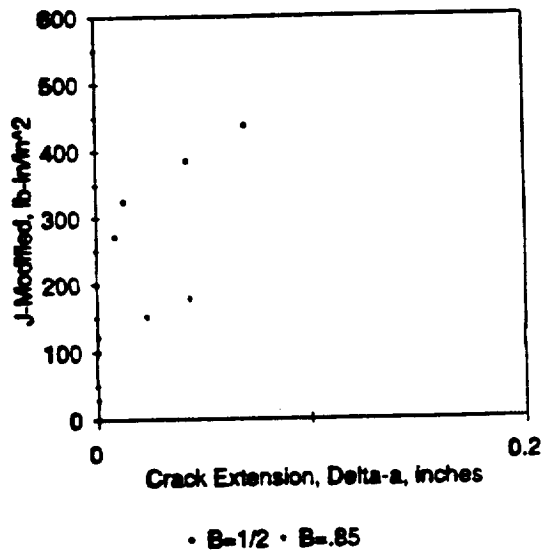


Figure 3.8: Qualified J_M R curves for AL6061-T651 specimens: (a) single-edge notched tension specimens of different ligament thicknesses, B , (or equivalently ligament proportions, R_L) with constant ligament length, $b = 1/2$ - inch, and (b) comparison of CT specimens with SENT specimens.

Qualified J_M R Data for AL6061-T651 Specimens

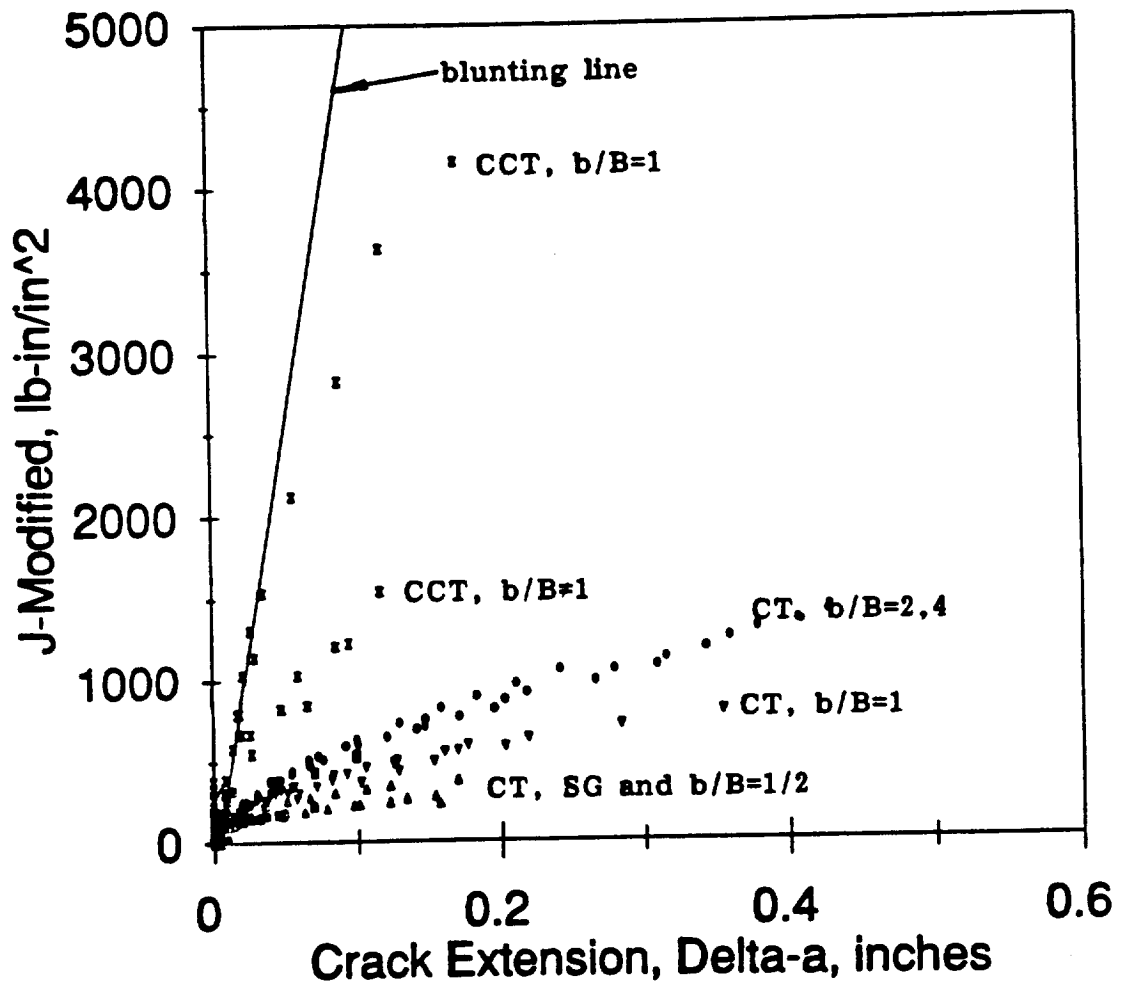


Figure 3.9: Qualified J_M R curves for AL6061-T651 specimens comparing CT, SENT, and CCT configurations.

Qualified J_M R Data for IN718-STA1 Center-Cracked Tension Specimens

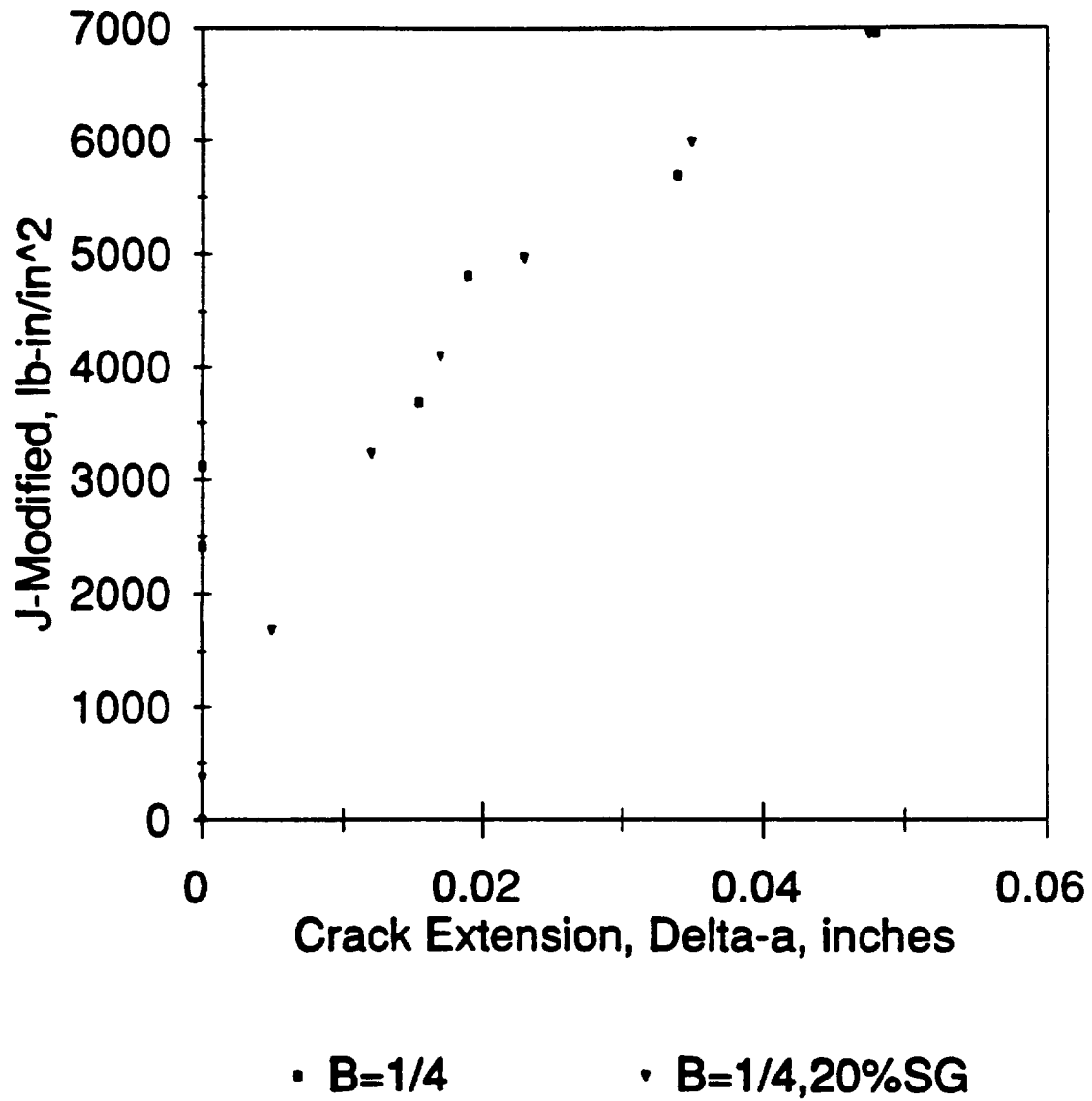


Figure 3.10: Qualified J_M R curves for IN718-STA1 center-cracked tension specimens comparing nonside-grooved to side-grooved configurations, $B = 1/4$ -inch.

Qualified $J_M R$ Data for IN718-STA1 Specimens

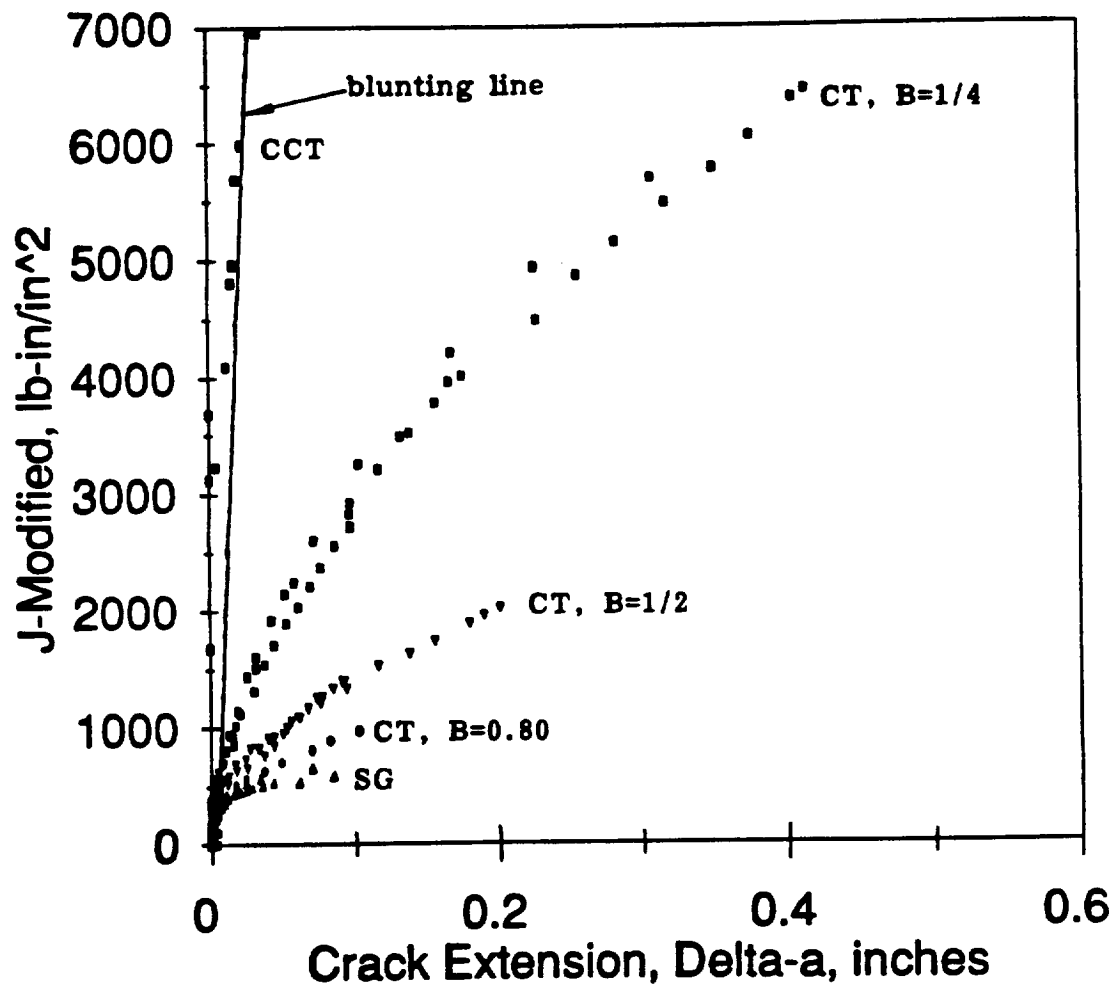


Figure 3.11: Qualified $J_M R$ curves for IN718-STA1 specimens comparing CT and CCT configurations.

Qualified J_M R Data for IN718-STA1 Compact Tension Specimens

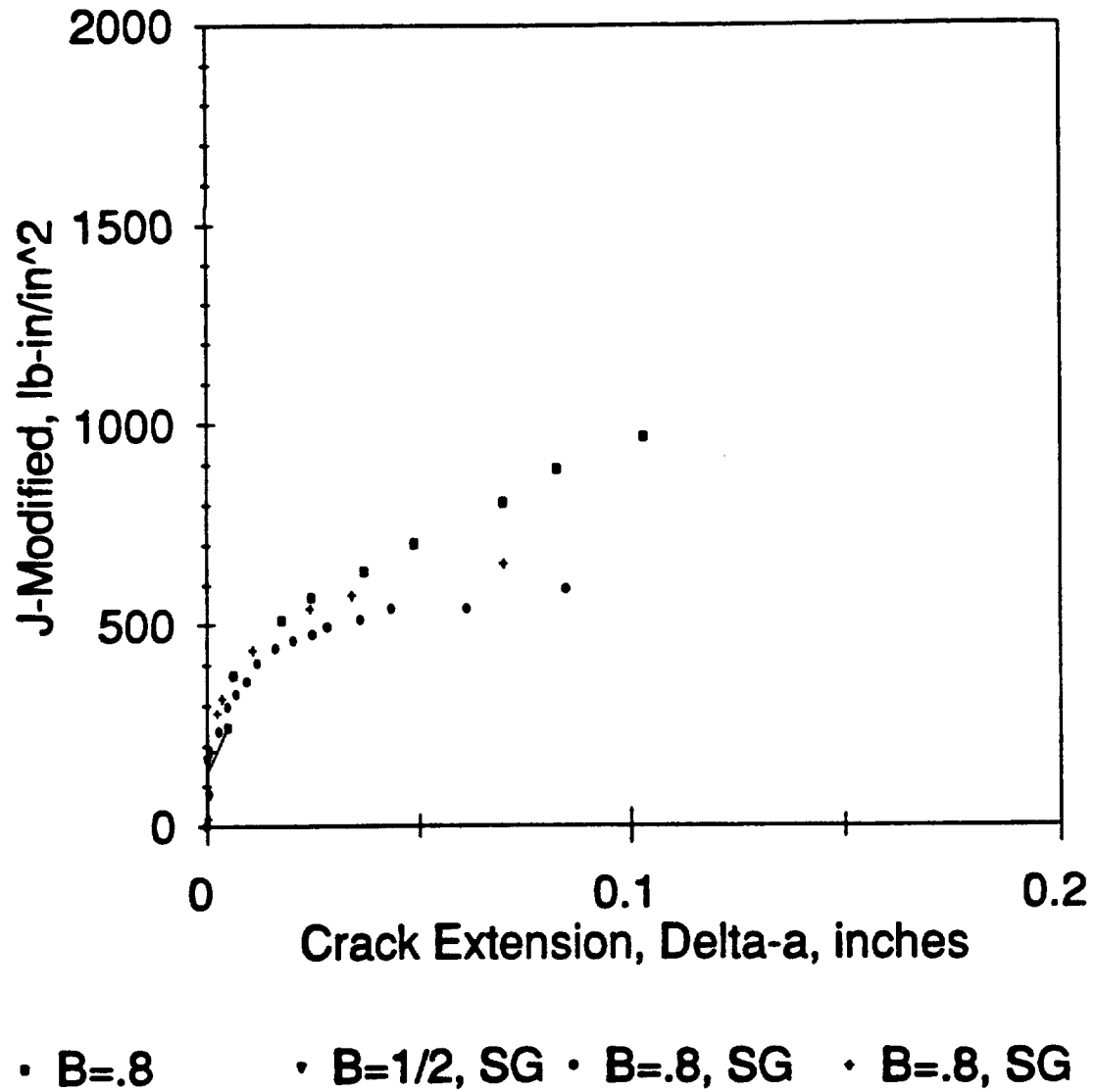


Figure 3.12: Collection of qualified J_M R curves for IN718-STA1 compact tension specimens comparing side-grooved condition to thickest ligament configuration, $B = 0.8$ -inches.

Qualified J_M R Data for IN718-STA1 Compact Tension Specimens

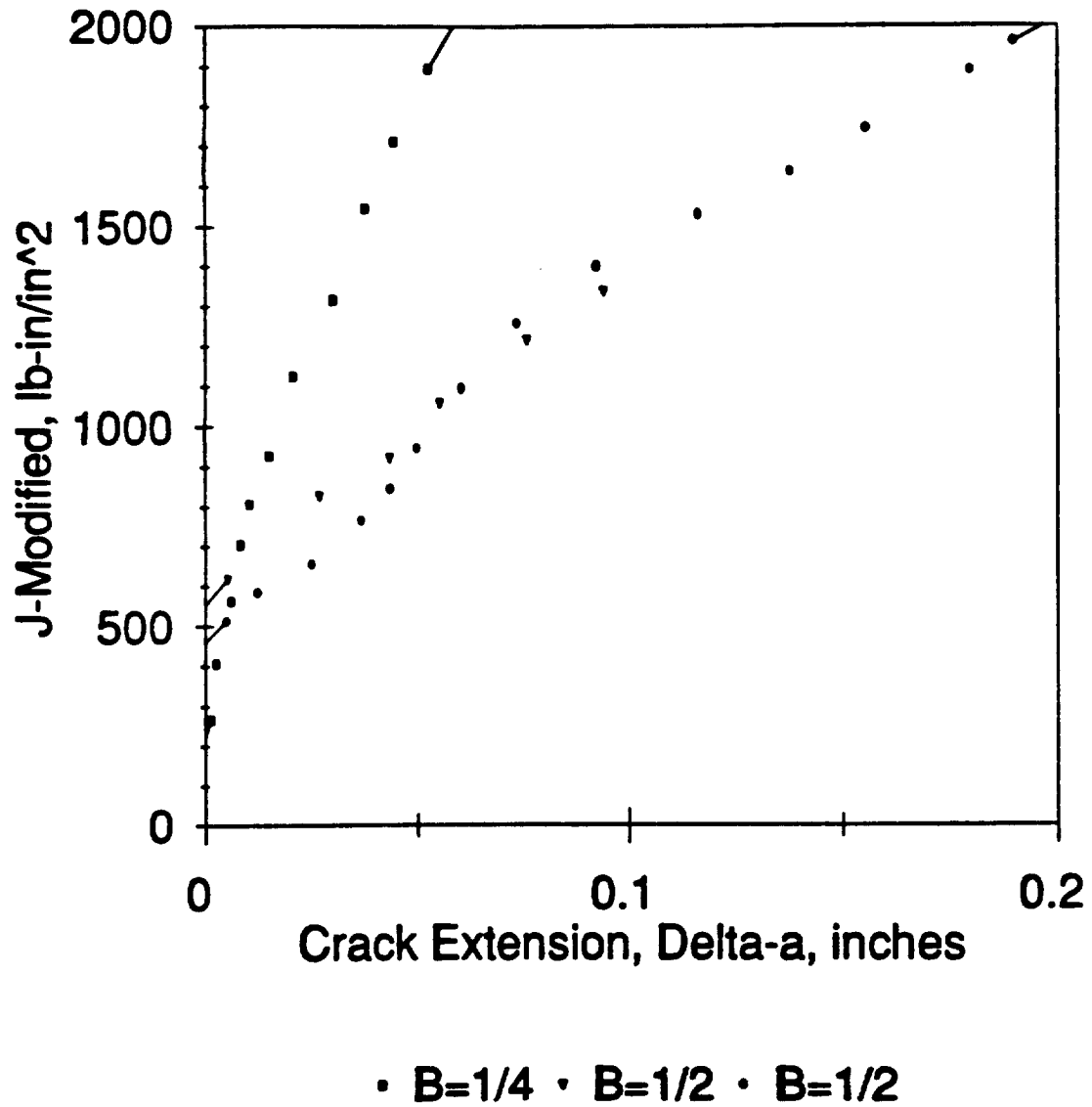


Figure 3.13: Collection of qualified J_M R curves for IN718-STA1 compact tension specimens comparing different ligament proportions, R_L .

J_R Curves and Regression Results

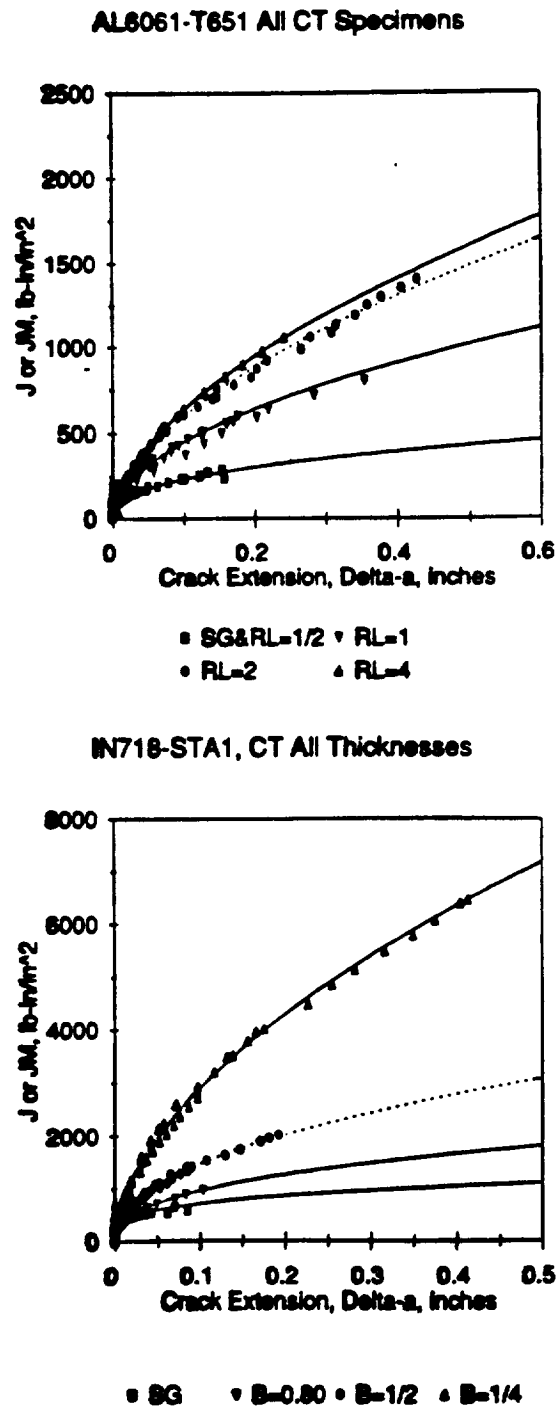


Figure 3.14: Results of regression analysis, power law fits, (a) AL6061-T651 CT specimens, and (b) IN718-STA1 CT specimens.